Phase-field modeling of cavity growth and dislocation climb

Benoit Dabas, Antoine Ruffini, Yann Le Bouar, Thomas Jourdan, Alphonse Finel

Phase-field modeling of cavity growth and dislocation climb

B. Dabas[a,b], A. Ruffini[a,*], Y. Le Bouar[a], T. Jourdan[b], A. Finel[a]

[a] *Université Paris-Saclay, ONERA, CNRS, Laboratoire d'étude des microstructures, 92322, Châtillon, France.*
[b] *Université Paris-Saclay, CEA, Service de Recherche en Corrosion et Comportement des Matériaux, SRMP, 91191, Gif-sur-Yvette, France*

Abstract

An original phase-field model coupling cavity growth, dislocation climb and vacancy diffusion is proposed. The model naturally accounts for elastic interactions between objects while its kinetic equations guarantee that matter is conserved when bulk vacancies are exchanged at the cavity surface or the dislocation core. An original spectral method that drastically reduces simulation time is also proposed in order to efficiently obtain the stationary vacancy concentration profiles during the objects evolution. It is shown how this model can be calibrated in a physically-informed way to reproduce diffusion-mediated cavity growth and dislocation climb under the so called "local equilibrium assumption". As an application of the model, the microstructural evolution of an annealed irradiated aluminum sample, implying interactions between several cavities and dislocations, is simulated. Non trivial effects regarding the dislocation-induced elastic interactions on the closure kinetics of cavities are notably highlighted.

Keywords: Phase-field, Cavity, Dislocation, Vacancy Diffusion, Elastic interactions, Irradiation

1. Introduction

In general, describing and predicting quantitatively the macroscopic behavior of metals and alloys requires reproducing the evolution of a microstructure composed of diverse objects (phases, precipitates, cavities, grain boundaries, dislocations, point defects, etc.) which evolve under the effect of multi-physics driving forces (chemical, mechanical, thermal, electrical, etc.). Both theoretically and numerically, phase-field methods have proven to be particularly relevant for this task, offering the possibility of describing multi-physics interactions within a common variational framework, at the characteristic space and time scale of the object dynamics [1, 2].

Using phase-field methods to reproduce diffusion-mediated cavity growth has been performed for about fifteen years, especially in the irradiated materials community where such objects are commonly observed [3]. Two classes of models are usually proposed. In models of class B (according to the nomenclature introduced in [4]), the conserved concentration field related to point defects is the unique field variable which is used to describe both species diffusion and cavities [5, 6, 7, 8, 9, 10, 11, 12, 13, 14, 15]. In models of class C, a non-conserved auxiliary field is introduced to represent cavities in addition to the conserved concentration fields [16, 17, 18, 19, 20, 21, 22, 23, 24, 25, 26, 27, 28, 29, 30, 31, 32, 33, 34]. Models of class C appear relevant for three reasons: (i) they allow for uncoupling the concentration profiles from the cavity surface energy and thus have a better control on this value; (ii) it makes the mechanical coupling of the cavity (and potentially others) distinct from that of the diffusive species; (iii) additional kinetic parameters are introduced which allows for controlling the reaction rate of point defects at the cavity surface, extending the modeling of their growth to processes that are not exclusively controlled by bulk diffusion.

In all of these phase-field simulations, the diffusion of vacancies is considered as the primary mechanism responsible of the cavity growth. In richest models however, the following phenomena are explicitly taken into account: diffusion of interstitials [6, 7, 19, 20, 18, 22, 23, 24, 26, 27, 28, 12, 29, 30, 14, 31, 15, 32, 33], presence of static grain boundaries [17, 18, 19, 20, 24, 25, 28, 33], diffusion of gas atoms linked to a pressure inside some cavities or bubbles [20, 18, 21, 24, 32], anisotropic surface energies [25, 26], surface stresses [13]... Except in a few studies [5, 21, 24, 28, 13, 15, 34], elastic effects are neglected as they are considered to

*Corresponding author
Email address: antoine.ruffini@onera.fr (A. Ruffini)

be second-order effects for diffusion-mediated cavity growth, especially when other extended defects generating internal stresses such as grain boundaries or dislocations are not explicitly taken into account. Furthermore, the dynamics of climbing dislocations and their elastic interactions with cavities are not taken into account while, in irradiated materials notably, such extended defects are likely to be formed concomitantly to cavities [35].

Phase-field formulations enabling to simulate diffusion-mediated dislocation climb have already been proposed in the literature [36, 37, 38, 39, 40, 41, 42, 43]. However, to our knowledge, they have never been coupled to cavity growth. Simulations developed specifically for this task are generally based on Cluster Dynamics [44, 45, 46, 47] or Object Kinetic Monte Carlo (OKMC) simulations [48, 49, 50] where strong hypotheses are necessarily considered. In both methods, systems are assumed dilute. In cluster dynamics simulations, systems are in addition assumed to be locally homogeneous, while elastic interactions are included through mean-field bias factors that make this method unable to describe the elasticity-induced evolution of dense heterogeneous microstructures. Although elastic interactions can be more precisely taken into account in OKMC [51], they are usually not considered. In [52], an approach based on the coupling between OKMC simulations and Discrete Dislocations Dynamics [53, 54, 55, 56] is proposed, allowing the authors to simulate the climb of a dislocation interacting with a precipitate. Such approaches require however to couple two-scales distinct methods (which can be numerically tricky and potentially time-demanding) while certain local rules introduced to account for the object kinetics are not constrained by the physical self-consistency of a variational formalism. Non-local models have also been proposed to simulate diffusion-mediated cavity growth and dislocation climb [57, 58]. Here again, they are based on necessary assumptions regarding the shape of objects, their spatial density and elastic interactions that are likely to be undermined by more precise descriptions such as the phase-field.

In light of this, we propose an original phase-field description that couples vacancy diffusion-mediated cavity growth and dislocation climb in a framework that naturally accounts for elastic interactions. The proposed model is notably based on a variational formulation inspired by some of our previous works [38, 40] which guarantees that matter is conserved when vacancies diffusing in the matrix are exchanged at the cavity surface or the dislocation core. Only vacancy diffusion is considered, but adding interstitial diffusion constitutes a relatively trivial extension which could be proposed in future works.

The phase-field model is exposed in the first part of the paper with some details of its numerical implementation. In particular, an original spectral method is presented enabling to efficiently obtain the stationary vacancy concentration profiles during the objects evolution. In a second part, simulations of the cavity closure and dislocation climb in simple geometries are performed and compared to known analytical solutions. These simulations demonstrate ability of the model to quantitatively describe diffusion-controlled processes. In a last part, we investigate the microstructural evolution of an annealed irradiated aluminum sample resulting from the interactions between several cavities and dislocations. Non trivial effects regarding the dislocation-induced elastic interactions on the closure kinetics of cavities are notably highlighted.

2. Phase-field model

In this section, the phase-field model coupling dislocation climb, cavity growth and vacancy diffusion is presented. This model naturally accounts for the elastic interactions between objects and guarantees through variational constraints that matter is conserved when vacancies are exchanged between objects and the matrix.

2.1. System and relevant fields

Cavities and dislocation loops are characterized by auxiliary fields (phase-fields) that account for their presence at a point $\boldsymbol{r} = (x, y, z)$ of the system (see Fig. 1) [2]. Cavities are represented by the field η such that $\eta(\boldsymbol{r}, t)$ evolves rapidly but smoothly from 0 within the matrix to 1 inside a cavity.

In general, dislocations can climb in different crystallographic planes and dislocation phase-fields ϕ_p can be defined in each type of climbing planes p. In this study however, only dislocations climbing in one plane will be considered, keeping in mind that the generalization of the formalism to several distinct planes is relatively straightforward. They are thus characterized by a unique two-dimensional field ϕ and a climb plane $(O; y, z)$ localized at x_0 such that:

$$\Phi(\boldsymbol{r}, t) = \phi(y, z, t)\delta(x - x_0), \tag{1}$$

where $\phi(y, z, t)$ varies between 0 in the matrix to n inside a loop, with $n \in \mathbb{Z}$. Here, n is a positive or negative integer accounting for the number of crystallographic planes respectively added or removed in each continuous plane. The delta Dirac function δ mathematically

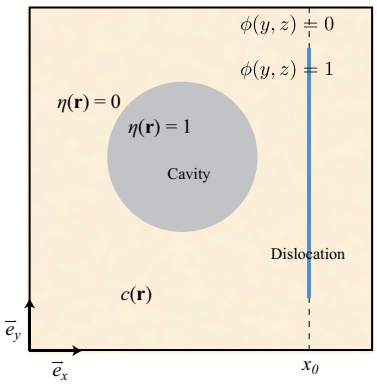

Figure 1: 2D scheme of a system containing a cavity and a dislocation dipole represented by their corresponding phase-field η and ϕ. The atomic vacancy concentration field c is defined everywhere in the system.

accounts for the dislocation confinement in its $x = x_0$ climbing plane.

Vacancies within the matrix are characterized by the concentration field c representing their lattice site fraction. This field is a real defined everywhere in the matrix, except in cavities where $c(\boldsymbol{r}, t)$ drops to zero. All of these objects are likely to generate local deformations and interact through elastic contributions. For this, the strain tensor field $\varepsilon_{ij}(\boldsymbol{r}, t)$ is also considered.

Cavities and dislocations grow or shrink only through an exchange of vacancies. In order to guarantee that the total amount of matter is conserved when vacancies are exchanged, a conservation law has to link η, ϕ and c that all account for non-occupied lattice site fraction. For this, extending the formulation introduced in [38, 40], a conserved field Ψ is introduced with the following definition:

$$\Psi(\boldsymbol{r}, t) = \eta(\boldsymbol{r}, t) + b\phi(y, z, t)\delta(x - x_0) + c(\boldsymbol{r}, t), \quad (2)$$

where b is the Burgers vector amplitude of dislocations. As it will be shown later, fields η and ϕ will be controlled by Allen-Cahn equations, while the evolution of c, which will be deduced from a Cahn-Hilliard equation imposed on the conserved field Ψ, will consist in a diffusion term completed by sources/sinks terms inherited from the conserved character of Ψ [38, 40].

2.2. Free energy functional

From now, the dependency of fields with $\boldsymbol{r}$ and t is omitted for clarity. At mesoscale, the total free energy of a system of finite volume V is given by :

$$\mathcal{F}\left(\{\eta\}, \{\phi\}, \{c\}, \{\varepsilon_{ij}\}\right) = \int_V \Big(f_{cav}(\eta) + f_{dis}(\phi) + f_{chem}(c, \eta) + f_{el}(\varepsilon_{ij}, \eta, \phi, c)\Big)\mathrm{d}V, \quad (3)$$

where f_{cav}, f_{dis} and f_{chem} are free energy densities related to the presence of cavities, dislocations and vacancies, respectively. f_{el} accounts for the elastic contributions.

The free energy density f_{cav} writes as the sum of a homogeneous contribution discriminating two states ($\eta = 1$ inside cavities and $\eta = 0$ outside) and a gradient term that makes the cavity surfaces described by a thin region where η passes diffusely from 0 to 1. In this work, the classical double-well homogeneous potential is used:

$$f_{cav}(\eta) = \frac{3\gamma}{4}\left(\frac{16\eta^2(1-\eta)^2}{\xi} + \xi|\boldsymbol{\nabla}\eta|^2\right), \quad (4)$$

where γ is the isotropic surface energy $[J.m^{-2}]$ and ξ the characteristic diffuse surface width $[m]$ of cavities. In what follows, the homogeneous term of this contribution will be specifically labeled $f_{cav}^{homo}(\eta) = 12\gamma\eta^2(1-\eta)^2/\xi$.

For dislocation loops, a similar formulation is adopted with two specificities: the homogeneous potential is infinitely degenerated (equals to zero when $\phi = n$, $n \in \mathbb{Z}$) and the gradient term must be projected in the climbing plane (here of normal $\boldsymbol{n} = \boldsymbol{e}_x$). According to [59, 60, 61] where this approach was developed for gliding dislocations, the following potential can be considered:

$$f_{dis}(\phi) = \frac{\pi\Gamma}{4}\left(\frac{\sin^2(\pi\phi)}{w} + w|\boldsymbol{n}\times\boldsymbol{\nabla}\phi|^2\right)\delta(x - x_0), \quad (5)$$

where Γ is the dislocation core energy $[J.m^{-1}]$ and w the characteristic core size $[m]$. The homogeneous term of this contribution is also labeled $f_{dis}^{homo}(\phi) = \pi\Gamma\sin^2(\pi\phi)/(4w)\,\delta(x - x_0)$.

The chemical free energy of vacancies takes two different forms depending on whether we are in the matrix or inside cavities. In the matrix, a dilute solution of vacancies where $c \ll 1$ can be assumed such that:

$$f_{chem}^{mat}(c) = \frac{E_f}{\Omega}c + \frac{k_B T}{\Omega}\Big(c\ln c + (1-c)\ln(1-c)\Big), \quad (6)$$

where E_f is the formation energy of a vacancy $[J]$, Ω the atomic volume $[m^3]$, $k_B = 1.38 \times 10^{-23} J.K^{-1}$ the Boltzmann constant and T the temperature $[K]$. If the vacancy concentration stays close to its equilibrium value,

one can perform an expansion at the lowest order of Eq. (6) and ultimately consider a free energy variation that reduces to:

$$f_{chem}^{mat}(c) = f_0 + \frac{k_B T}{2\Omega c_0}(c - c_0)^2, \tag{7}$$

where c_0 is given by

$$c_0 = \exp\left(-\frac{E_f}{k_B T}\right) \tag{8}$$

while $f_0 = f_{chem}^{mat}(c_0)$.

Inside cavities, a similar form of chemical energy is postulated:

$$f_{chem}^{cav}(c) = f_0 + \mathcal{K}\frac{k_B T}{2\Omega c_0}c^2, \tag{9}$$

which guarantees that matrix and cavities are at equilibrium when their concentration are given by $c = c_0$ and $c = 0$, respectively. In this expression, $\mathcal{K}$ is a positive non-dimensional parameter introduced to control the curvature of the chemical free energy density inside cavities, relatively to that of the matrix. The precise role of this parameter and the choice of relevant values will be discussed in the next section.

The chemical free energy of vacancies thus has to depend on the field η which indicates locally whether we are in the matrix ($\eta = 0$) or inside cavities ($\eta = 1$). In this work, the following expression is chosen:

$$f_{chem}(c,\eta) = \frac{k_B T}{2\Omega c_0}\Big[(\mathcal{K}-1)h(\eta)+1\Big]\Big[c - c_0(1-h(\eta))\Big]^2, \tag{10}$$

where $h(\eta) = 3\eta^2 - 2\eta^3$ is a monotonic interpolation function such that $h(0) = h'(0) = h'(1) = 0$ and $h(1) = 1$ [62]. Note also that, as it plays no role in the equilibrium nor in the driving forces that enter into kinetics, the constant term f_0 appearing in Eqs. (7) and (9) has been set to zero. Then, it is straightforward to verify that in the matrix $f_{chem}(c,0) = f_{chem}^{mat}(c)$, and in a cavity $f_{chem}(c,1) = f_{chem}^{cav}(c)$. In Fig. 2, the sum $f_{cav}^{homo}(\eta) + f_{chem}(c/c_0,\eta)$ is plotted as a function of both c/c_0 and η for $\mathcal{K} = 5$. As expected, this homogeneous energy density landscape presents two minima at $(c/c_0 = 0, \eta = 1)$ and $(c/c_0 = 1, \eta = 0)$.

The elastic free energy density is given by the generalized Hooke's law:

$$f_{el}(\varepsilon_{ij},\eta,\phi,c) = \frac{1}{2}\sigma_{ij}(\eta,\phi,c)\Big(\varepsilon_{ij} - \varepsilon_{ij}^0(\phi,c)\Big) - \sigma_{ij}^A\langle\varepsilon_{ij}\rangle, \tag{11}$$

where σ_{ij} is the stress tensor:

$$\sigma_{ij}(\eta,\phi,c) = \lambda_{ijkl}\Big(1-h(\eta)\Big)\Big(\varepsilon_{kl} - \varepsilon_{kl}^0(\phi,c)\Big), \tag{12}$$

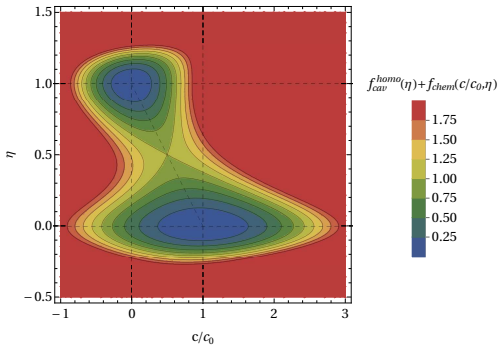

Figure 2: Homogeneous energy density landscape controlling η and c/c_0. Along the trajectory $\eta + c/c_0 = 1$ there is an energy barrier which is here normalized to one.

with λ_{ijkl} the stiffness tensor of the matrix, σ_{ij}^A the applied stresses, $\langle\varepsilon_{ij}\rangle$ the average strains and ε_{ij} the linearized strain field related to the gradient of displacements u_i by:

$$\varepsilon_{ij} = \frac{1}{2}\left(\frac{\partial u_i}{\partial x_j} + \frac{\partial u_j}{\partial x_i}\right). \tag{13}$$

Note that we use here implicit summations over repeated indices.

In Eqs. (11) and (12), ε_{ij}^0 is the eigenstrain tensor that account for the local deformations introduced by both dislocations and vacancies:

$$\varepsilon_{ij}^0(\phi,c) = \varepsilon_{ij}^p\delta(x - x_0)h(\phi) + \varepsilon_{ij}^v c. \tag{14}$$

In this expression, the first term is related to dislocations $\varepsilon_{ij}^p = -b\delta_{i1}\delta_{j1}$ where b is the Burgers vector norm and δ_{ij} the Kronecker symbol [1]. $h(\phi) = \phi - \sin(2\pi\phi)/(2\pi)$ is another interpolation function related to ϕ such that $h(n) = n$ and $h'(n) = h''(n) = 0$ with $n \in \mathbb{Z}$ [63]. In Eq. (14), the second term is related to an isostatic eigenstrain induced by a vacancy $\varepsilon_{ij}^v = V^*\delta_{ij}/(3\Omega)$ where V^* is the relaxation volume and Ω the atomic volume. In Eq. (14), it is assumed that this contribution is linearly dependent of the concentration field following the usual Vegard's law [64].

2.3. Kinetics

Non-conserved phase-fields η and ϕ are supposed to follow the usual Allen-Cahn equations while, in order to conserve matter, the conserved field Ψ introduced in

[1] The dislocation eigenstrain accounts for a contraction of amplitude b, perpendicular to the $x = x_0$ planes: $\delta_{ij} = \delta_{i1}$.

Eq. (2) is supposed to follow a Cahn-Hilliard equation [65, 66]:

$$\dot{\eta} = -L_\eta \frac{\delta \mathcal{F}^*}{\delta \eta}, \tag{15}$$

$$\dot{\phi} = -L_\phi \frac{\delta \mathcal{F}^*}{\delta \phi}, \tag{16}$$

$$\dot{\Psi} = \boldsymbol{\nabla} \cdot \left(M \boldsymbol{\nabla} \frac{\delta \mathcal{F}^*}{\delta \Psi} \right). \tag{17}$$

In these equations, $\mathcal{F}^*\left(\{\eta\}, \{\phi\}, \{\Psi\}, \{\varepsilon_{ij}\}\right)$ is the total free energy expressed in terms of fields η, ϕ, Ψ and ε_{ij}. L_η and L_ϕ are kinetic coefficients of the non-conserved phase-fields and M is the mobility of Ψ (which is likely to depend on the local value of the fields). The physical meaning of M is discussed further below.

In order to express the kinetic equation directly in terms of η, ϕ, c and ε_{ij}, we simply have to note that $\mathcal{F}^*\left(\{\eta\}, \{\phi\}, \{\Psi\}, \{\varepsilon_{ij}\}\right)$ is nothing but $\mathcal{F}\left(\{\eta\}, \{\phi\}, \{c\}, \{\varepsilon_{ij}\}\right)$ as given in Eq. (3) through the change of variable provided by Eq. (2). Similarly to what is done for dislocation climb in [38, 40], the following set of kinetic equations can then be established:

$$\dot{\eta} = -L_\eta \left(\frac{\delta \mathcal{F}}{\delta \eta} - \frac{\delta \mathcal{F}}{\delta c} \right), \tag{18}$$

$$\dot{\phi} = -L_\phi \left(\frac{\delta \mathcal{F}}{\delta \phi} - b \frac{\delta \mathcal{F}}{\delta c} \delta(x - x_0) \right), \tag{19}$$

$$\dot{c} = \boldsymbol{\nabla} \cdot \left(M \boldsymbol{\nabla} \frac{\delta \mathcal{F}}{\delta c} \right) - b\dot{\phi}\delta(x - x_0) - \dot{\eta}, \tag{20}$$

which shows that M is nothing but the vacancy mobility, which can be assumed to depend on the concentration field c. Terms $b\dot{\phi}\delta(x - x_0)$ and $\dot{\eta}$ then turn out to be source or sink terms for the vacancy field c in Eq. (20). Mobilities L_η and L_ϕ are related to the reaction rate between fields η and c at cavity surfaces, or ϕ and c in dislocation cores [38, 40].

Diffusion-controlled kinetics being slow, the average strain $\langle \varepsilon_{ij} \rangle$ and the strain field ε_{ij} (or displacements fields u_i) are obtained by imposing the mechanical equilibrium:

$$\langle \boldsymbol{\sigma} \rangle = \boldsymbol{\sigma}^A, \tag{21}$$

$$\boldsymbol{\nabla} \cdot \boldsymbol{\sigma} = 0, \tag{22}$$

where $\boldsymbol{\sigma}^A$ is the applied stress of components σ^A_{ij}, $\boldsymbol{\sigma}$ the stress tensor whose components are given in Eq. (12) and $\langle \boldsymbol{\sigma} \rangle$ its spatial average. These mechanical equations are efficiently solved in Fourier space thanks to the Fast Fourier Transforms (FFT) numerical libraries and the iterative strategy detailed in [67, 68]. In the present work, the solver introduced in [69] is used as it is shown to tackle very efficiently and without any artifacts the infinite stiffness contrast between the matrix and cavities. For the sake of brevity, details of these spectral methods are not included in this work.

In a dilute system, when the vacancy concentration c stays close to its equilibrium value $c_0 \ll 1$ as assumed in this study, one can consider that M is constant and given by:

$$M = \frac{\Omega D_v}{k_B T} c_0, \tag{23}$$

where D_v is the vacancy diffusivity involved in the usual Fick equation [70, 40]. The diffusivity depends on temperature according to:

$$D_v = D_0 \exp\left(-\frac{E_m}{k_B T} \right), \tag{24}$$

where E_m is the vacancy migration energy and D_0 the T-independent pre-exponential factor [71].

Furthermore, as will be justified later, it is considered in this work that the evolution of the vacancy concentration field c is quasi-static with the evolution of cavities and dislocations. As a consequence, one gets $\dot{c} = 0$ leading to this final set of evolution equations (at mechanical equilibrium):

$$\dot{\eta} = -L_\eta \left(\frac{\delta \mathcal{F}}{\delta \eta} - \frac{\delta \mathcal{F}}{\delta c} \right), \tag{25}$$

$$\dot{\phi} = -L_\phi \left(\frac{\delta \mathcal{F}}{\delta \phi} - b \frac{\delta \mathcal{F}}{\delta c} \delta(x - x_0) \right), \tag{26}$$

$$0 = M\nabla^2 \left(\frac{\delta \mathcal{F}}{\delta c} \right) - b\dot{\phi}\delta(x - x_0) - \dot{\eta}. \tag{27}$$

2.4. Numerical implementation

When simulations are performed, periodic cubic systems of size $(L_x, L_y, L_z) \in \left(\mathbb{R}_0^+\right)^3$ are considered and discretized in space with the help of a regular cubic grid of spacing d $[m]$ such that $(N_x, N_y, N_z) = (L_x, L_y, L_z)/d \in \mathbb{N}_0^3$. The value of d is chosen such that cavities and dislocations are individually resolved. It thus depends on the relevant space scale of a given problem. Hence, the coordinates $\boldsymbol{r} = (x, y, z)$ are replaced by their discrete version (l, m, n) d with $l = 0, 1, ..., N_x - 1$; $m = 0, 1, ..., N_y - 1$ and $n = 0, 1, ..., N_z - 1$.

The dimensionless forms of Eqs. (25 – 27) are obtained by considering an energy density f_0 and a time unit τ that turn out to be natural for the model. Since it is intended to describe mechanisms that are controlled by

vacancy diffusion, the following units are considered:

$$f_0 = \frac{k_B T}{\Omega}, \tag{28}$$

$$\tau = \frac{t_0}{c_0} \text{ with } t_0 = \frac{d^2}{D_v}. \tag{29}$$

With these definitions, discretized dimensionless parameters given in Tab. 1 can be defined.

Energy densities and time		
$\tilde{f}_{\text{label}} = f_{\text{label}}/f_0$	$\tilde{\lambda}_{ijkl} = \lambda_{ijkl}/f_0$	$\tilde{t} = t/\tau$
Lengths and strains		
$\tilde{\boldsymbol{r}} = \boldsymbol{r}/d = (l, m, n)$	$\tilde{u}_i = u_i/d$	$\tilde{\varepsilon}_{ij} = \varepsilon_{ij}$
Operators		
$\Pi(l - l_0) = d\,\delta(x - x_0)$	$\tilde{\boldsymbol{\nabla}} = d\,\boldsymbol{\nabla}$	$\tilde{\boldsymbol{\nabla}}^2 = d^2\,\boldsymbol{\nabla}^2$
Cavities		
$\tilde{\gamma} = \gamma/(f_0 d)$	$\tilde{\xi} = \xi/d$	
Dislocations		
$\tilde{\Gamma} = \Gamma/(\lambda_{44} b^2)$	$\tilde{w} = w/d$	$\tilde{b} = b/d$
Vacancies		
$\tilde{c} = c/c_0$		
Mobilities		
$\tilde{L}_\eta = L_\eta d^2/M$	$\tilde{L}_\phi = L_\phi d^3/M$	

Table 1: Discretized dimensionless parameters of the model. Π is the discrete rectangular function of width d defined by $\Pi(l - l_0) = 1$ if $l = l_0$ and $\Pi(l - l_0) = 0$ if $l \neq l_0$. λ_{44} is the shear elastic constant λ_{ijij} of an elastically cubic system in Voigt notation.

The discretized dimensionless forms of Eqs. (25 – 27) can thus be written as:

$$\frac{\partial \eta}{\partial \tilde{t}} = -\tilde{L}_\eta \left(\frac{\partial \tilde{f}_{tot}^{homo}}{\partial \eta} - \frac{3}{2}\tilde{\gamma}\tilde{\xi}\tilde{\nabla}^2\eta - \frac{\partial \tilde{f}_{tot}^{homo}}{\partial c} \right), \tag{30}$$

$$\frac{\partial \phi}{\partial \tilde{t}} = -\tilde{L}_\phi \left(\frac{\partial \tilde{f}_{tot}^{homo}}{\partial \phi} - \frac{\pi}{2}\tilde{\Gamma}\tilde{w}\tilde{\lambda}_{44}\tilde{b}^2\tilde{\nabla}^2_{mn}\phi - \tilde{b}\frac{\partial \tilde{f}_{tot}^{homo}}{\partial c}\bigg|_{l=l_0} \right), \tag{31}$$

$$0 = \tilde{\nabla}^2 \left(\frac{\partial \tilde{f}_{tot}^{homo}}{\partial c} \right) - \tilde{b}\frac{\partial \phi}{\partial \tilde{t}}\Pi(l - l_0) - \frac{\partial \eta}{\partial \tilde{t}}, \tag{32}$$

where $\tilde{f}_{tot}^{homo} = \tilde{f}_{cav}^{homo} + \tilde{f}_{dis}^{homo} + \tilde{f}_{chem} + \tilde{f}_{el}$ represents the homogeneous contribution of the total free energy density. These equations are subsequently expressed in the discretized dimensionless Fourier space defined by the following transformations:

$$\left\{ \mathrm{f}(\tilde{\boldsymbol{r}}) \right\}_{\tilde{\boldsymbol{k}}} = \mathrm{f}(\tilde{\boldsymbol{k}}) = \frac{1}{N_x N_y N_z} \sum_{l=0}^{N_x-1} \sum_{m=0}^{N_y-1} \sum_{n=0}^{N_z-1} \mathrm{f}(\tilde{\boldsymbol{r}}) e^{-i\tilde{\boldsymbol{k}}\cdot\tilde{\boldsymbol{r}}}, \tag{33}$$

$$\left\{ \mathrm{f}(\tilde{\boldsymbol{k}}) \right\}_{\tilde{\boldsymbol{r}}} = \mathrm{f}(\tilde{\boldsymbol{r}}) = \sum_{l=0}^{N_x-1} \sum_{m=0}^{N_y-1} \sum_{n=0}^{N_z-1} \mathrm{f}(\tilde{\boldsymbol{k}}) e^{i\tilde{\boldsymbol{k}}\cdot\tilde{\boldsymbol{r}}}, \tag{34}$$

where $\tilde{\boldsymbol{k}} = 2\pi(\frac{l}{N_x}, \frac{m}{N_y}, \frac{n}{N_z})$ with $l = 0, 1, ..., N_x - 1$; $m = 0, 1, ..., N_y - 1$ and $n = 0, 1, ..., N_z - 1$. This Fourier implementation, which in this work relies upon the FFTW library [72], allows us to integrate in time Eqs. (30) and (31) by using a simple semi-implicit Euler scheme:

$$\eta(\tilde{\boldsymbol{k}}, \tilde{t} + \delta\tilde{t}) = \frac{\eta(\tilde{\boldsymbol{k}}) - \delta\tilde{t}\,\tilde{L}_\eta \left\{ \frac{\partial \tilde{f}_{tot}^{homo}}{\partial \eta} - \frac{\partial \tilde{f}_{tot}^{homo}}{\partial c} \right\}_{(\tilde{\boldsymbol{k}},t)}}{1 + 3\,\delta\tilde{t}\,\tilde{L}_\eta\,\tilde{\gamma}\,\tilde{\xi}\,\tilde{\boldsymbol{k}}^2/2}, \tag{35}$$

$$\phi(\tilde{\boldsymbol{k}}, \tilde{t} + \delta\tilde{t}) = \frac{\phi(\tilde{\boldsymbol{k}}) - \delta\tilde{t}\,\tilde{L}_\phi \left\{ \frac{\partial \tilde{f}_{tot}^{homo}}{\partial \phi} - \tilde{b}\frac{\partial \tilde{f}_{tot}^{homo}}{\partial c}\Big|_{l=l_0} \right\}_{(\tilde{\boldsymbol{k}},t)}}{1 + \pi\,\delta\tilde{t}\,\tilde{L}_\eta\,\tilde{\Gamma}\,\tilde{w}\,\tilde{\lambda}_{44}\,\tilde{b}^2\,\left(\tilde{k}_m^2 + \tilde{k}_n^2\right)/2}. \tag{36}$$

In Fourier space, solving Eq. (32) to find $\tilde{c}(\tilde{\boldsymbol{k}}, \tilde{t} + \delta\tilde{t})$ is straightforward since an iterative spectral method can be set up (identical in spirit to that involved in the mechanical solver). For this, the homogeneous driving forces in real space are rewritten in the following generic form:

$$\frac{\partial \tilde{f}_{tot}^{homo}}{\partial c} = \alpha_1 \tilde{c} + G_1(\tilde{c}) + G_2, \tag{37}$$

$$\frac{\partial \tilde{f}_{tot}^{homo}}{\partial \eta} = \alpha_3 \tilde{c} + G_3(\tilde{c}) + G_4, \tag{38}$$

where α_1 and α_3 are constants linking linearly $\tilde{c}$ to their respective driving forces. The odd indexed functions G_1 and G_3 are $\tilde{c}$-dependent contributions that will be actualized during the iterative procedure, and the even indexed functions G_2 and G_4 are $\tilde{c}$-independent contributions that will stay fixed during the iterative procedure. According to the energy densities introduced in subsection 2.2, the following choice can be proposed:

$$\alpha_1 = N\langle g_1 \rangle, \tag{39}$$

$$G_1(\tilde{c}) = (g_1 - \alpha_1)\,\tilde{c}, \tag{40}$$

$$G_2 = g_1\,(h(\eta) - 1) - \frac{\tilde{\sigma}_{ij} V^*}{3\Omega}\delta_{ij}, \tag{41}$$

and:

$$\alpha_3 = N\langle g_3\rangle, \tag{42}$$

$$G_3(\tilde{c}) = (g_3 - \alpha_3)\,\tilde{c} + c_0\frac{\mathcal{K}-1}{2}h'(\eta)\tilde{c}^2, \tag{43}$$

$$G_4 = \frac{\partial \tilde{f}_{cav}^{homo}}{\partial \eta} + \frac{\partial \tilde{f}_{el}}{\partial \eta} + c_0\frac{h(\eta)-1}{2}\left(3g_1 - \mathcal{K}\right)h'(\eta), \tag{44}$$

where $g_1 = (\mathcal{K}-1)\,h(\eta)+1$ and $g_3 = c_0\,(2g_1 - \mathcal{K})\,h'(\eta)$ are convenient intermediate functions, and N is an arbitrary positive number chosen to guarantee that the iterative strategy converges. Empirically, a good convergence is obtained for $N = \mathcal{K}$. It is recalled that $\langle\square\rangle$ designates the spatial average of the corresponding quantity. At each new time step, the value of $\tilde{c}(\tilde{\boldsymbol{k}}, \tilde{t}+\delta\tilde{t})$ is computed with the iterative algorithm presented in Alg. 1 in which the following global $\tilde{c}$-independent function is used:

$$\begin{aligned}\left\{G_6\right\}_{\tilde{\boldsymbol{k}}} = &-\tilde{\boldsymbol{k}}^2\left\{G_2\right\}_{\tilde{\boldsymbol{k}}} \\ &+ \tilde{L}_\phi\tilde{b}\left[\left\{\frac{\partial \tilde{f}_{tot}^{homo}}{\partial\phi} - \tilde{b}G_2\right\}_{\tilde{\boldsymbol{k}}} + \frac{\pi}{2}\tilde{\Gamma}\tilde{w}\tilde{\lambda}_{44}\tilde{b}^2\left(\tilde{k}_m^2 + \tilde{k}_n^2\right)\phi(\tilde{\boldsymbol{k}})\right] \\ &+ \tilde{L}_\eta\left[\left\{G_4 - G_2\right\}_{\tilde{\boldsymbol{k}}} + \frac{3\tilde{\gamma}\tilde{\xi}}{2}\tilde{\boldsymbol{k}}^2\eta(\tilde{\boldsymbol{k}})\right].\end{aligned} \tag{45}$$

In this model, the physical parameters are imposed. The surface width ξ and core size w are chosen such that the phase-field profiles are diffusely regularized with respect to the grid spacing. In practice, one will take $\xi = w = 4d$ which has been checked to be a relevant choice [73]. In the next section, it is shown how the remaining unknown parameters $\mathcal{K}$, $\tilde{L}_\eta$ and $\tilde{L}_\phi$ can be chosen to simulate diffusion-controlled processes in a physically justified way. The efficiency of the proposed time-integration method (in terms of maximal reachable time step $\delta\tilde{t}$) is also discussed.

3. Validation of the model in simple cases

In this part, the shrinkage of a single cavity and the climb of a dislocation dipole are simulated. Numerical results regarding their kinetics and field profiles are compared to analytical solutions derived from asymptotic analysis of the model. This study allows us to select relevant values for $\mathcal{K}$, $\tilde{L}_\eta$ and $\tilde{L}_\phi$ to quantitatively simulate diffusion-controlled processes.

3.1. Cavity shrinkage: choosing $\mathcal{K}$ and $\tilde{L}_\eta$

The 2D system described in Fig. 3 is considered. It corresponds to a cylindrical cavity of radius R, embedded in a matrix where the vacancy concentration is fixed at $c_\infty < c_0$ on an external cylinder of radius $R_\infty > R$.

Algorithm 1 Iterative algorithm used to determine $\tilde{c}(\tilde{\boldsymbol{k}}, \tilde{t}+\delta\tilde{t})$. The convergence is reached when maximum of the concentration driving force at each point of the system is below "toler" $\ll 1$.

Require: $\eta(\tilde{\boldsymbol{k}}, \tilde{t}+\delta\tilde{t}), \phi(\tilde{\boldsymbol{k}}, \tilde{t}+\delta\tilde{t}), \tilde{c}(\tilde{\boldsymbol{k}}, \tilde{t}), \tilde{c}(\tilde{\boldsymbol{r}}, \tilde{t})$

preparation: $\alpha_1, \alpha_3, \left\{G_6\right\}_{(\tilde{\boldsymbol{k}}, \tilde{t}+\delta\tilde{t})}$

initialize: $\left\{G_{1(3)}(\tilde{c}^{n=0})\right\}_{\tilde{\boldsymbol{r}}} \xrightarrow{FT} \left\{G_{1(3)}(\tilde{c}^{n=0})\right\}_{\tilde{\boldsymbol{k}}}$

loop

$$\begin{aligned}\left\{\frac{\delta\mathcal{F}}{\delta c}\right\}_{\tilde{\boldsymbol{k}}}^{n} = &-\left[\tilde{\boldsymbol{k}}^2 + \tilde{L}_\phi\tilde{b}^2 - \tilde{L}_\eta\left(\frac{\alpha_3}{\alpha_1} - 1\right)\right]\alpha_1\tilde{c}^n(\tilde{\boldsymbol{k}}) \\ &- \left[\tilde{\boldsymbol{k}}^2 + \tilde{L}_\phi\tilde{b}^2 + \tilde{L}_\eta\right]\left\{G_1(\tilde{c}^n)\right\}_{\tilde{\boldsymbol{k}}} + \tilde{L}_\eta\left\{G_3(\tilde{c}^n)\right\}_{\tilde{\boldsymbol{k}}} \\ &+ \left\{G_6\right\}_{\tilde{\boldsymbol{k}}}\end{aligned}$$

$\left\{\frac{\delta\mathcal{F}}{\delta c}\right\}_{\tilde{\boldsymbol{k}}}^{n} \xrightarrow{FT^{-1}} \left\{\frac{\delta\mathcal{F}}{\delta c}\right\}_{\tilde{\boldsymbol{r}}}^{n}$

if $\left[\max_V\left(\left|\frac{\delta\mathcal{F}}{\delta c}\right|^n\right) \leq \text{"toler"}\right]$ **then**

  exit

else

$$\tilde{c}^{n+1}(\tilde{\boldsymbol{k}}) = \frac{-\left[\tilde{k}^2 + \tilde{L}_\phi\tilde{b}^2 + \tilde{L}_\eta\right]\left\{G_1(\tilde{c}^n)\right\}_{\tilde{\boldsymbol{k}}} + \tilde{L}_\eta\left\{G_3(\tilde{c}^n)\right\}_{\tilde{\boldsymbol{k}}} + \left\{G_6\right\}_{\tilde{\boldsymbol{k}}}}{\left[\tilde{k}^2 + \tilde{L}_\phi\tilde{b}^2 - \tilde{L}_\eta\left(\frac{\alpha_3}{\alpha_1} - 1\right)\right]\alpha_1}$$

$\tilde{c}^{n+1}(\tilde{\boldsymbol{k}}) \xrightarrow{FT^{-1}} \tilde{c}^{n+1}(\tilde{\boldsymbol{r}})$

Boundary Conditions on $\tilde{c}$ in real space

$\left\{G_{1(3)}(\tilde{c}^{n+1})\right\}_{\tilde{\boldsymbol{r}}} \xrightarrow{FT} \left\{G_{1(3)}(\tilde{c}^{n+1})\right\}_{\tilde{\boldsymbol{k}}}$

end if

end loop

In the asymptotic analysis performed in Appendix A, the radial velocity of the cavity v is given by Eq. (A.24) while profiles of the chemical potential μ write as Eqs. (A.8) that depend on the surface chemical potential μ_{surf} given Eq. (A.25). These solutions of v and μ_{surf} depend on the mobility L_η. Formally, this parameter can be calibrated to the reaction rate of vacancies at cavity surface, provided that a suitable model can be identified to the phase-field formalism. In this work however, the so-called local equilibrium condition is considered, consisting in assuming that vacancies are at equilibrium along the interfaces and therefore that the surface movement is solely limited by the vacancy flux. Hence, the cavity/matrix exchange of vacancies is assumed to be instantaneous such that $L_\eta \to +\infty$. In this case, solutions of v and μ_{surf} do not depend on L_η anymore. According to Eq. (A.24) in 2D, we can see that this condition is fulfilled when $R\ln(R_\infty/R) \gg 2M/\left(3\xi L_\eta\right)$. This

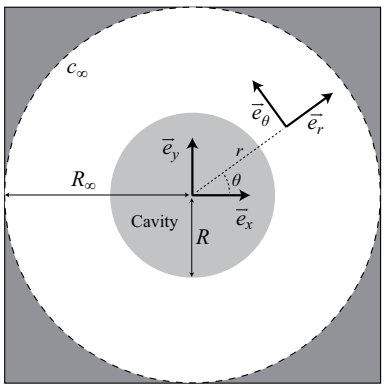

Figure 3: Cavity shrinking under a flux of vacancies.

allows us to simplify the radial velocity to:

$$v = \frac{-D_v\,(c_0 - c_\infty) - M\frac{\gamma}{R}}{R\ln\left(R_\infty/R\right)}, \tag{46}$$

and the surface chemical potential to:

$$\mu_{surf} = \frac{\gamma}{R}. \tag{47}$$

By putting this expression of μ_{surf} in Eqs. (A.8), one gets the explicit solutions for the chemical potential inside and outside the cavity. Now, since it is shown in Appendix A that $\eta = \eta_{eq}$ with:

$$\eta_{eq}(r) = \frac{1}{2}\left(1 + \tanh\left(\frac{2(R-r)}{\xi}\right)\right), \tag{48}$$

it can be considered, provided the cavity radius R is large enough, that μ inside the cavity is given by Eq. (A.3) with $\eta = 1$, while outside it is given by Eq. (A.3) with $\eta = 0$. In this case, one obtains the following 2D concentration profile:

$$\begin{aligned} r \le R \;&:\; c(r) = c^-, \\ r > R \;&:\; c(r) = c_\infty + (c_\infty - c^+)\,\frac{\ln\left(r/R_\infty\right)}{\ln\left(R_\infty/R\right)}, \end{aligned} \tag{49}$$

where c^- and c^+ are the concentrations on both sides of the surface given by $c^- = d_0/(\mathcal{K}R)$ and $c^+ = c_0 + d_0/R$ with the capillary length d_0 defined by $d_0 = \Omega c_0\gamma/(k_BT) = M\gamma/D_v$. One can thus notice that:

$$c^- = \frac{c^+ - c_0}{\mathcal{K}}, \tag{50}$$

showing that the constant concentration of vacancies inside the cavity is controlled by its supersaturation near the surface on matrix side, through parameter $\mathcal{K}$. This supersaturation near the surface characterizes the well-known Gibbs-Thomson effect. To guarantee that the model maintains a concentration of vacancies close to zero in the cavity despite of this effect, we should thus have $\mathcal{K} \to +\infty$. Since numerically infinite $\mathcal{K}$ values cannot be considered, sufficiently high but finite values must be envisaged. We therefore systematically tested the influence of different $\mathcal{K}$ values (from 10 to 100), as well as different values of time step δt, on the closure rate of an isolated cavity. In these tests (see Appendix C in [74]) we found that, with an acceptable error of a few percent on the closure rate compared with that obtained with the most accurate parameters, the choice of $\mathcal{K} = 10$ allows to consider $\delta t = 10^{-3}\tau$, while a smaller order of magnitude time step has to be considered with $\mathcal{K} = 100$. In the following, the value $\mathcal{K} = 10$ is therefore chosen, as it is a very good fidelity/effectiveness compromise limiting the accumulation of vacancies inside cavities.

As shown before, to perform simulations in which the local equilibrium assumption applies, it is necessary to take sufficiently large values of $\tilde{L}_\eta = L_\eta d^2/M$ guaranteeing that $R\ln\left(R_\infty/R\right) \gg 2M/\left(3\xi L_\eta\right)$. In the finite size simulations that we will carry out, we can consider that in the worst case we have $R_\infty \approx 10R$ and $R \approx \xi$, with $\xi = 4d$. This leads to:

$$R\ln\left(\frac{R_\infty}{R}\right) \gg \frac{2M}{3\xi L_\eta} \Rightarrow \tilde{L}_\eta \gg 0.018. \tag{51}$$

Numerically, the finite value $\tilde{L}_\eta = 1$ is considered.

In this work, we consider that the vacancies follow a quasi-static kinetics with respect to the dislocation field (see Eq. 27). This is a valid approximation in the case of a moderate driving force [75, 38]. In addition, the quasi-static relaxation of the vacancy concentration field with respect to the cavity field can be deduced as follows. First, Eq. (49) shows that the steady-state profile of the concentration field in the vicinity of the cavity spreads over a characteristic length L_v which is of the order of R. Therefore, the characteristic time necessary for the vacancy diffusion over this distance is $t_v \approx R^2/D_v$. Second, the velocity of the surface, estimated from the shrinkage of an isolated cavity in an equilibrium matrix is to first order $v \approx -M\gamma/R^2$ (see Eq. (46)). Combining the above two points and using Eq. (23), it appears that the movement of the surface during the characteristic relaxation time of the diffusion field vt_v is of the order of the capillary length d_0. In our simulations, d_0 is of the order of 10^{-7}nm, i.e. orders of magnitude smaller than the characteristic diffusion length $L_v \approx R$, implying that the vacancy concentration field can be assumed quasi-static with respect to the cavity field η.

3.2. Cavity shrinkage: simulation

The shrinkage of the 2D cavity is now simulated with the aim of comparing its closure rate v and profiles of c/c_0 and η to the theoretical ones. For this, we consider a cavity of initial radius $R_{t=0} = 32$ nm in a pure aluminum crystal of surface energy $\gamma = 1$ J.m^{-2} [76, 77]. Geometry and initial/boundary conditions of the simulations are that of Fig. 3 with $c_\infty = 0.8c_0$ at $R_\infty = 64$ nm. Elasticity is neglected. The thermokinetic vacancy parameters are given in Tab. 2. By considering a temperature of $T = 473.15$ K, one has $c_0 = 7.30 \times 10^{-8}$ and $D_v = 3.18 \times 10^{-12}$ m^2.s^{-1} according to Eqs. (8) and (24), respectively. With these data, the capillary length is $d_0 = 1.86 \times 10^{-7}$ nm.

Formation energy E_f	0.67 eV
Migration energy E_m	0.61 eV
Pre-exponential factor D_0	1×10^{-5} m^2.s^{-1}
Atomic volume Ω	16.6 Å^3
Relaxation volume V^*	-0.38 Ω

Table 2: Thermokinetic vacancy parameters in pure Aluminum [78, 79, 80, 38, 81, 82].

The simulation parameters are given in Tab. 3. The phase-field mobility $\tilde{L}_\eta$ and the parameter $\mathcal{K}$ are chosen in consistency with the previous subsection (local equilibrium assumption and no vacancies inside the cavity). It turns out that the value of $\mathcal{K}$ that we have retained for our simulations is close to the choice of parameter which plays a similar role in [16].

Grid spacing d	1 nm
Surface width ξ	4 nm
Phase-field mobility $\tilde{L}_\eta$	1
Relative chemical curvature $\mathcal{K}$	10
$\dot{c} = 0$ convergence criterion "toler"	10^{-3}
Time-step $\delta\tilde{t}$	10^{-3}

Table 3: Simulation parameters for the cavity shrinkage in pure aluminum.

In Fig. 4, the evolution of $R(t)$ extracted from the simulation is compared to the theoretical value provided by the numerical integration of Eq. (46). These curves are found to be close to each other. Notably, they exhibit closure rates v (slopes of the curves) with discrepancies less than 5% as long as the radius is bigger than the diffuse width of the surface W. This typical width can be evaluated by considering the length over which the phase-field passes from $\phi = 0.01$ to $\phi = 0.99$. According to Eq. (48), one can calculate $W = \xi\,\mathrm{artanh}\,(2\times0.99-1) = 2.3\xi = 9.2$ nm which is consistent with the diffuse profiles shown in Fig. 5. The remaining discrepancy between the curves may be attributed to the hypothesis of the asymptotic analysis where the surface concentration jump is set to $\Delta c^{surf} = c^+ - c^- = c_0$ despite the Gibbs-Thomson effect.

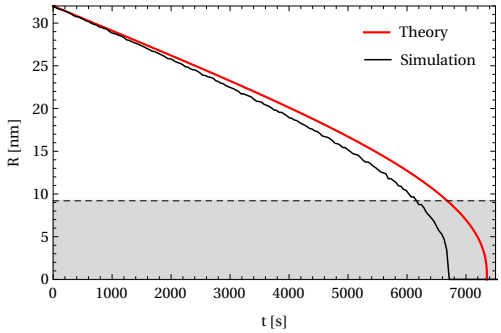

Figure 4: Radius of the cavity versus time. The gray region corresponds to irrelevant cases where the cavity radius R becomes smaller than the diffuse surface width $W = 9.2$ nm.

In Fig. 5, the evolution of fields η and c/c_0 extracted from the simulation is displayed during the cavity shrinkage, for different values of its radius R. Profiles of the fields are compared to theoretical ones provided by Eqs. (48) and (49), respectively. A remarkable concordance can be pointed out. Notably, the vacancy supersaturation at the pore surface characterizing the Gibbs-Thomson effect is quantitatively well reproduced, concomitantly with the c profile in the matrix side. Inside the cavity, a constant amount of vacancies c^- can be measured. Its value nearly perfectly matches the theoretical value predicted by Eq. (50) indicating that c^- is a fraction $1/\mathcal{K}$ of the surface supersaturation. As it can be observed, the choice of $\mathcal{K} = 10$ leads to a value of vacancy concentration inside the cavity that remains very close to zero during almost the entire shrinkage of the cavity. It is worth mentioning that such a simulation has also been performed in 3D. The results are not shown here but has led to very similar conclusions.

Here is an important point that must be highlighted. Usually, the time integration of the kinetic equation controlling the concentration field c is performed concomitantly with the kinetic equations controlling the evolution of other fields. Numerically, the combined evolu-

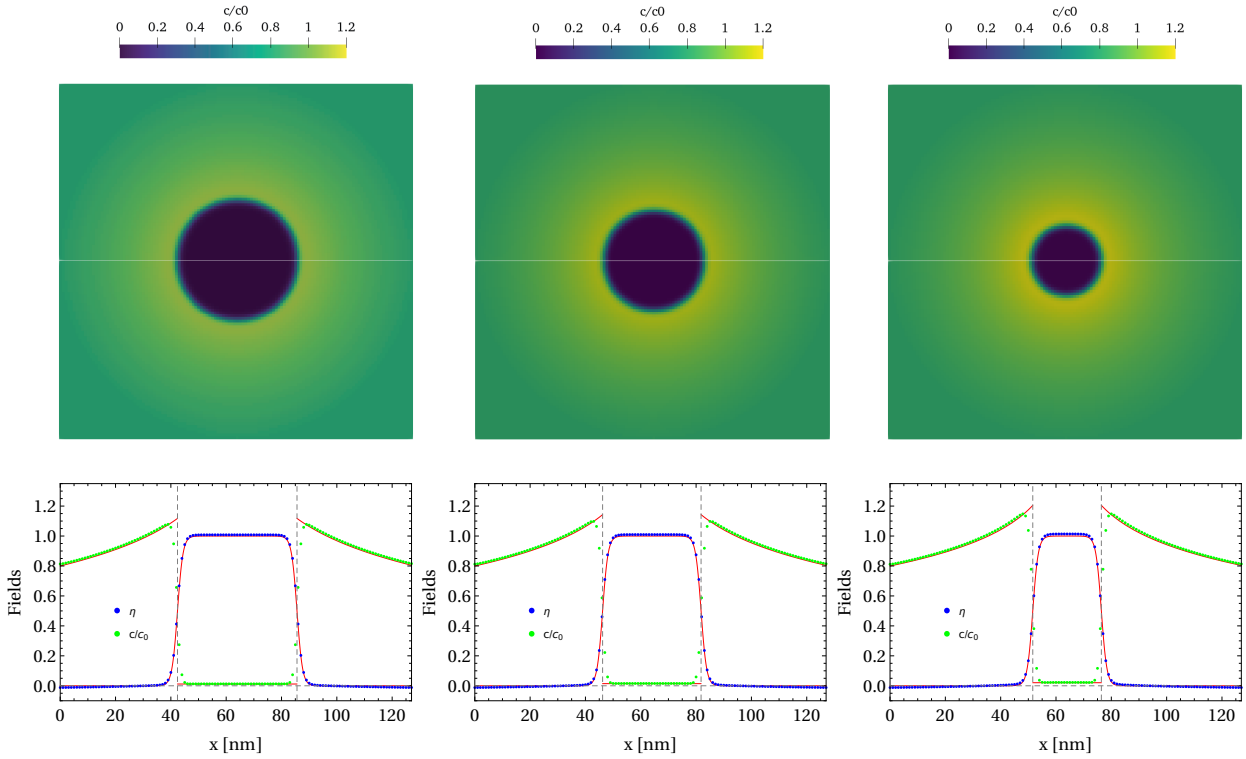

(a) R=21.6 nm (b) R=17.8 nm (c) R=12.4 nm

Figure 5: (Top) c/c_0 vacancy concentration field during the cavity shrinkage. (Bottom) Profiles of η and c/c_0 over the line displayed on top pictures. Point data correspond to the values extracted from the simulation while red thin lines correspond to the theoretical profiles of η and c/c_0 provided by Eqs. (48) and (49), respectively (see colors on-line). Theoretical profiles are plotted with the simulation cavity radius.

tion of fields is thus limited by the smaller time scale which is generally $t_0 = d^2/D_v$ related to the characteristic time of diffusion over the grid spacing d. Hence, if Eq. (32) had to be explicitly integrated (by taking $\dot{c} \neq 0$), time-steps of the order of $0.1t_0$ would have been required (see for example [6]). Instead, by using the fixed-point algorithm presented in Alg. 1, a time-step of $\delta t = 10^{-3}\tau \approx 10^4 t_0$ has been used to perform the cavity shrinkage simulation and validate the model. With parameters displayed in Tab. 3, we found that except for the very first iterations, Alg. 1 updates the vacancy concentration field in an average of only 0.5 iteration at each time-step, with a computational cost in terms of user-time that remains in the same order of magnitude compared to an explicit time-integration algorithm. As a consequence, we observed a gain of five orders of magnitude to integrate the evolution equations and simulate the cavity shrinkage, without altering quantitatively its closure kinetic. We believe this is a important milestone to simulate coupled diffusion problems that notably made possible the simulations and statistical analysis exposed in Sec. 4 of this paper.

3.3. Dislocation climb: choosing L_ϕ

Following the approach adopted previously to quantify the shrinkage of a cavity, the climb of a dislocation dipole is now investigated. The system is described in Fig. 6. It consists in two dislocations embedded in a rectangular matrix where the vacancy concentration is fixed at c_∞ on the boundaries and on a stripe localized at $y = L_y/2$. A constant applied stress σ^A_{ij} is considered such that $\sigma^A_{ij} = \sigma^A_{11}\delta_{i1}\delta_{j1}$.

In the asymptotic analysis performed in Appendix B, the climb velocity v is given by Eq. (B.15) while the radial profile of the chemical potential writes as Eqs. (B.9) that depend on the core chemical potential μ_{core} given Eq. (B.16). These solutions are obtained by assuming that each dislocation core, whose radius is noted r_0, remains at the center of circular diffusion domain whose radius is R_∞. In the initial condition, this radius can be related to $L_x/2$ in consistency with the simulation geometry. The formal expressions of v and μ_{core} depend on L_ϕ which is a parameter that could be identified to the reaction rate of vacancies in the dislocation core by linking the equations of an ad hoc model to the

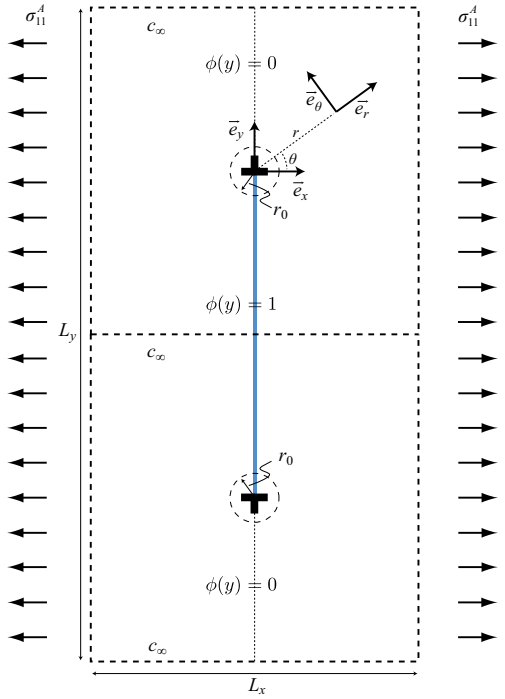

Figure 6: Dislocation climbing under the effect of both vacancy flux and applied stress.

phase-field ones [40]. That said, under the local equilibrium hypothesis such as assumed in this work, it can be considered that the core/matrix exchange of vacancies is instantaneous: $L_\phi \to +\infty$. In this case, the dislocation climb is controlled by vacancy diffusion with solutions of v and μ_{core} that must not depend on L_ϕ. According to Eq. (B.15), one should consequently consider that $\ln(R_\infty/r_0) \gg 4M/\left(wL_\phi b^2\right)$, simplifying the climb rate to:

$$v = \frac{2\pi D_v c_0}{b \ln(R_\infty/r_0)} \left(\frac{c_\infty}{c_0} - 1 - \frac{\Omega \sigma^A_{11}}{k_B T} \right), \tag{52}$$

and the core chemical potential to:

$$\mu_{core} = \sigma^A_{11}. \tag{53}$$

In Appendix B, the phase-field profile is assumed to be at equilibrium:

$$\phi_{eq}(y) = 1 - \frac{2}{\pi} \arctan\left(\exp\left(\frac{\pi y}{w} \right) \right). \tag{54}$$

To formulate explicitly the radial concentration profile around the cores, we just have to introduce the solution $\mu_{core} = \sigma^A_{11}$ in Eq. (B.9), and derive the solution of c by using the expression of the free energy Eq. (10) when $\eta = 0$. This leads to:

$$c(r) = c_\infty + (c_\infty - c_{core}) \frac{\ln(r/R_\infty)}{\ln(R_\infty/r_0)}, \tag{55}$$

where c_{core} is the vacancy concentration in the core region:

$$c_{core} = c_0 \left(1 + \frac{\Omega \sigma^A_{11}}{k_B T} \right). \tag{56}$$

This core concentration is nothing but the value classically considered in the dislocation literature when the chemical potential is linearized and local equilibrium assumed [83].

Here, for the local equilibrium assumption to be valid, one should take a value of $\tilde{L}_\phi = L_\phi d^3/M$ such that $\ln(R_\infty/r_0) \gg 4M/\left(wL_\phi b^2\right)$. In the finite size simulations that we will carry out, we can consider that $\ln(R_\infty/r_0) \approx 1$ is almost constant with $w = 4d$. This gives:

$$\tilde{L}_\phi \gg \frac{1}{\tilde{b}^2}. \tag{57}$$

Numerically, when $\tilde{b} = b/d = 1$, the value $\tilde{L}_\phi = 10$ can be considered to simulate diffusion-controlled dislocation climb, as already shown in [38].

3.4. Dislocation climb: simulation

The simulations are performed by considering a constant concentration c_∞ on the Cartesian boundaries of the box of size $L_x \times L_y = 15\,\text{nm} \times 30\,\text{nm}$, and on a stripe localized at $y = 15$ nm (see Fig. 6). The thermokinetic vacancy parameters are that of Tab. 2. As in Sec. 3, $T = 473.15$ K, $c_0 = 7.30 \times 10^{-8}$ and $D_v = 3.18 \times 10^{-12}$ $\text{m}^2.\text{s}^{-1}$. Here, the relaxation volume of vacancies is neglected ($V^* = 0$) such as assumed in the asymptotic analysis. Dislocation and elastic properties are provided in Tab. 4. The core energy is taken high enough such that the profile of ϕ remains mainly controlled by the dislocation contributions of the free energy despite its coupling with elastic and chemical terms. This choice does not alter the physics of dislocation climb in 2D systems but might be questionable in 3D simulations, when dislocations become curved and core energy contributes to the driving force (see Eq. (26)).

Burgers vector b	0.234 nm
Core energy Γ	$\lambda_{44} b^2$
Elastic coeff. λ_{11}, λ_{12}, λ_{44}	108 ; 61 ; 29 GPa

Table 4: Dislocation and elastic properties in pure Aluminum [83]. (The three cubic elastic constants are given in Voigt notation.)

The simulation parameters are given in Tab. 5. The phase-field mobility $\tilde{L}_\phi$ has been chosen according to the local equilibrium hypothesis. The parameter "toler" and $\delta\tilde{t}$ involved in Eq. (36) and Alg. 1 have been chosen under the requirement of a good fidelity/effectiveness compromise.

Grid spacing $d = b$	0.234 nm
Core size w	0.936 nm
Phase-field mobility $\tilde{L}_\phi$	10
$\dot{c} = 0$ convergence criterion "toler"	10^{-3}
Time-step $\delta\tilde{t}$	10^{-4}

Table 5: Simulation parameters for the dislocation climb in pure aluminum.

In Fig. 7, the numerical climb rate is compared to the theoretical value of v given Eq. (52) for several applied stresses σ^A_{11} or boundary concentrations c_∞. In Eq. (52), the geometrical term $\ln(R_\infty/r_0)$ is taken as a free fitting parameter to account for the fact that, in the simulations, boundary concentrations c_∞ are applied on straight boundaries and not on circles of radius R_∞ centered on dislocation cores as assumed in the theory. For this, we used the $v(\sigma^A_{11})$ curve of Fig. 7.a that corresponds to the case where only the applied stress has an influence on the climbing rate. It turns out that the fitting value 2.49 is found to be very close to 2.08 that would be calculated with the natural choice $R_\infty = L_x/2 = 7.5$ nm and $r_0 = w = 0.936$ nm. In both cases, a good agreement is found showing that the phase-field model quantitatively reproduces the kinetics of dislocation climb. Of course, the agreement is better with the $v(\sigma^A_{11})$ curve of Fig. 7.a since $\ln(R_\infty/r_0) = 2.49$ is fitted on this curve.

In Fig. 8, the evolution of fields ϕ, σ_{11}/λ_{44} and c/c_0 extracted from the simulation is displayed during the dislocation climb in the case $\sigma^A_{11} = 300$ MPa and $c_\infty = c_0$, when the distance separating dislocations is about 17 nm. Profiles of fields ϕ and c/c_0 are compared to theoretical ones provided by Eqs. (54) and (55), respectively. As for the the cavity shrinkage, a very good agreement can be found bearing witness to the quality of the simulation results.

In these validation simulations, the time-step is $\delta t = 10^{-4}\tau \approx 10^3 t_0$ while it would be in the order of $0.1t_0$ if $\dot{c}$ would have to be explicitly integrated. With parameters displayed in Tab. 3, except for the very first iterations, we found that Alg. 1 updates the vacancy concentration field in an average of 10 iterations at each time-step. As a consequence, compared to a classical time-integration, we observe that the effectiveness of our algorithm is increased by three order of magnitude in terms of user-time. In the present case, the gain in terms of effectiveness due to the implementation of a fixed point algorithm on $\dot{c}$ is not as high as in the cavity case. This is because $L_\phi = 10L_\eta$, which means that the time-step has to be reduced by the same amount, and also because the fixed point algorithm is one order of magnitude slower to converge in the dislocation case. Nevertheless, this result is a major improvement allowing us to access a much more extended simulation time range compared to some of our previous works [38, 40].

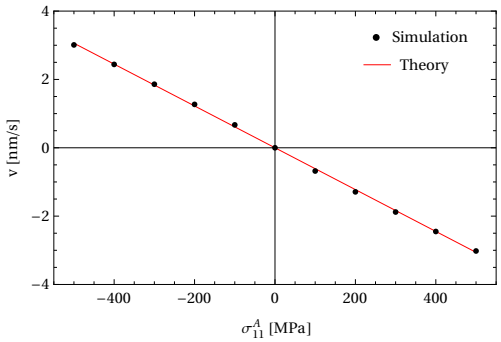

(a) Climbing rate versus applied stress.

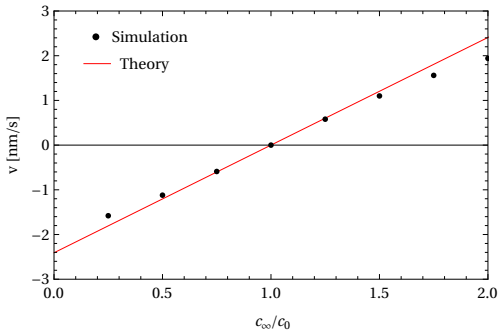

(b) Climbing rate versus boundary concentration.

Figure 7: Climbing rates extracted from the simulations (black point) compared to the theoretical values (red line) predicted by Eq. (52) when $\ln(R_\infty/r_0) = 2.49$.

4. Study of the annealing of an aluminum sample after irradiation

As a direct application of the model, we investigate the microstructural evolution of an annealed irradiated aluminum sample resulting from the interactions between cavities and dislocations.

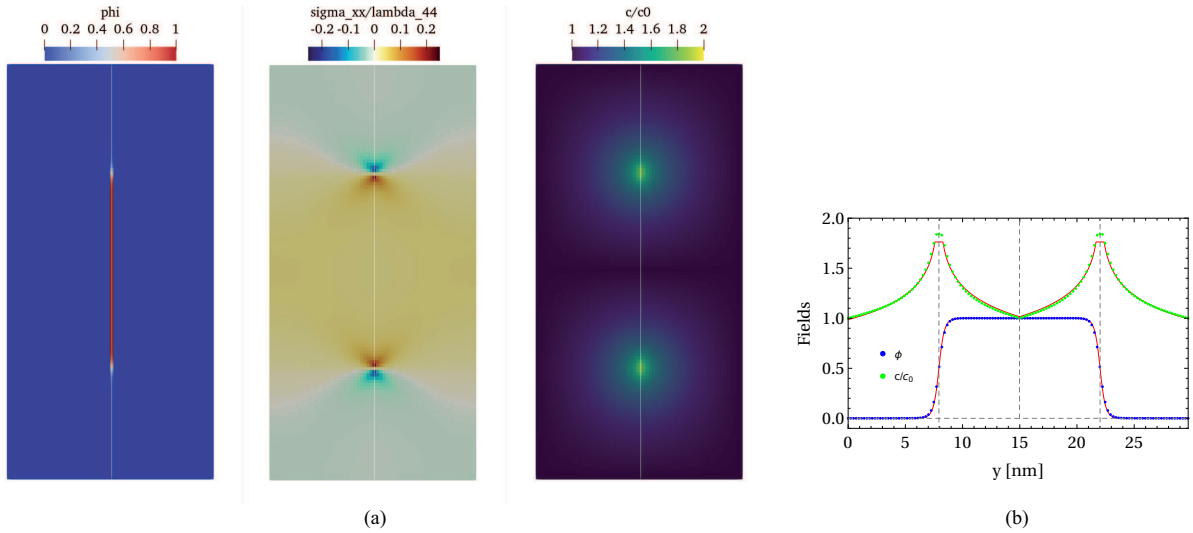

Figure 8: (a) Fields ϕ, σ_{11}/λ_{44} and c/c_0 during dislocation climb in the case $\sigma^A_{11} = 300$ MPa and $c_\infty = c_0$, when the distance separating dislocations is about 17 nm. (b) Profiles of ϕ and c/c_0 along the vertical line displayed in pictures (a). Point data correspond to the values extracted from the simulation while red thin lines correspond to the theoretical profiles of ϕ and c/c_0 provided by Eqs. (B.6) and (55), respectively. For the theoretical profile of c/c_0 we have considered $R_\infty = L_x/2 = 9.12$ nm and $r_0 = 0.4$ nm. (see colors on-line)

4.1. Experimental context and simulation set-up

The initial microstructure is typical of those observed in thin films of aluminum irradiated by electrons at high dose rate and high doses, of the order of a few displacements per atom [82]. A mixture of cavities and large dislocation loops are present in the foil, with approximately ten times more cavities than loops. Accordingly, we consider a 2D square system of side $L = 102.4$ nm, as shown in Fig. 9. We choose to simulate a population of $n_{cav} = 10$ cavities with an identical initial radius $R = 2$ nm. One dislocation loop of initial length $\ell = 12$ nm is also introduced. Because of the periodic boundary conditions, the dislocation dipole may be viewed as a vacancy loop in parts of the climbing plane where $\phi = 1$ or an interstitial loop in parts of the plane where $\phi = 0$. Hence, this second view is adopted to represent the interstitial loop which will be now cited as is (see Fig. 9). The matrix is initially placed at chemical equilibrium with $c = c_0$. All the physical properties of the system are that considered previously and provided in Tabs. 3 and 5.

Numerically, because of the size and densities of objects that we want to consider, a grid spacing of $d = 0.1$ nm is adopted with still characteristic surface and dislocation core sizes given by $\xi = w = 4d$. For numerical efficiency, a non dimensional time-step $\delta\tilde{t} = 10^{-3}$ is finally considered while the $\dot{c} = 0$ convergence criterion remains fixed to 10^{-3}.

In what follows, the microstructure evolution and kinetics of cavities and dislocations are addressed statistically in order to highlight their average mutual influence, independently of their positions. For this, 100 simulations of the aforementioned system are performed, with cavities and dislocation initially placed at random positions. The collapse rates of 1000 cavities and 100 interstitial dislocation loops are thus extracted.

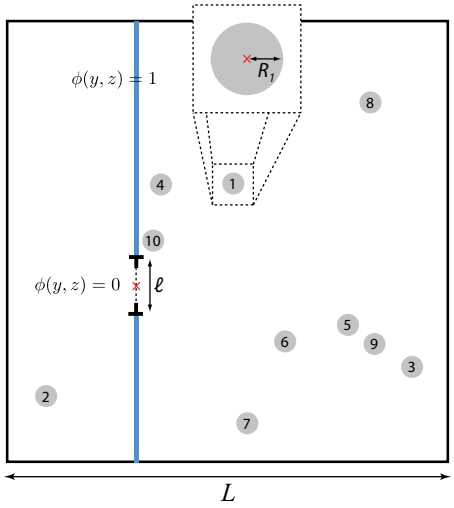

Figure 9: Initial set up for a typical simulation. Cavities are gray discs numbered from $i = 1$ to 10 with radius R_i. In 2D, the interstitial dislocation loop is a dipole of length ℓ represented by the dotted line where ϕ remains initialized to 0. The center of objects are indicated by a red cross. (See colors on-line)

4.2. Preliminary simulations, microstructure evolution

Before performing simulations of the complete microstructure, the collapse of a single isolated cavity of initial radius $R = 2$ nm is simulated in order to have a reference velocity for the subsequent kinetic analysis. For this, the simulation performed in Sec. 3 is reproduced by considering $c_\infty = c_0$ at the boundary of a circle of radius $R_\infty = R_{cut}$, where $R_{cut} = 10$ nm. This choice, which will be explained in the next paragraph, corresponds to approximately half the average distance between first neighbor cavities within the set of microstructures that will be studied next.

Evolution of the cavity radius as a function of time is shown in Fig. 10. To obtain a reference closure rate (slope of the curve), a linear fit is performed between 1 and 2 seconds, leading to $v_0 = 0.11$ nm/s. This procedure has been checked to be relevant for obtaining a low noised instantaneous-like closure rate at $t = 2s$. In the following, this procedure will by applied for all cavities of the complete microstructure.

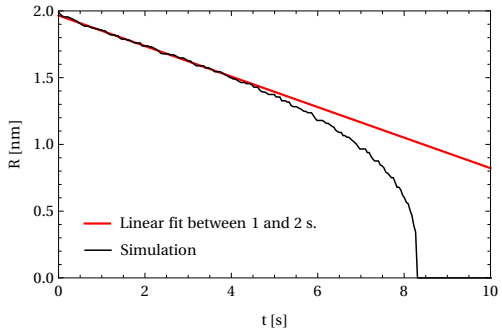

Figure 10: Radius of the reference isolated cavity versus time.

Then, we have compared in Fig. 11 the time evolution of the ten cavity radii R_i and the dislocation dipole length ℓ for one of the 100 simulations, by considering the two following reduced time steps: $\delta\tilde{t} = 10^{-3}$ and $\delta\tilde{t} = 10^{-4}$. As mentioned previously, $\delta\tilde{t} = 10^{-3}$ is considered in this Section although a ten times smaller time-step would be preferred to quantitatively reproduce the climb rate of the dislocation dipole (see Sec. 3). In Fig. 11, it can be seen that tendencies of the dotted curved obtained with $\delta\tilde{t} = 10^{-4}$ are found to be very similar to that of the solid curves obtained with $\delta\tilde{t} = 10^{-3}$. In particular, despite the fact that slopes of the dislocation curves between 1 and 2 seconds differ of about 11%, it is found that the discrepancy between slopes of the cavity curves over the same interval is in an average of about 2%. This means that the closure rate of cavities is marginally affected by this choice, justifying the use of $\delta\tilde{t} = 10^{-3}$ for all the simulations. This has allowed us to get the subsequent results regarding the closure kinetics of cavities in a reasonable time of about one week instead of ten.

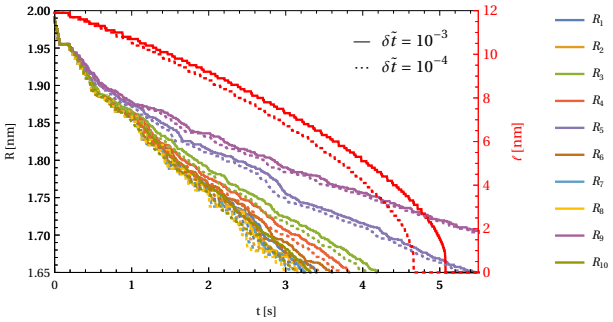

Figure 11: Radii of cavities (R_i to read on the left axis) and dislocation dipole length (ℓ in red to read on the right axis) versus time for one of the 100 simulations. (See colors on-line)

In Fig. 12, different snapshots of this simulation are shown as the time increases, highlighting the collapse of cavities and the dipole annihilation. In the top row of Fig. 12 presenting the vacancy concentration field, it is observed that cavities act a sources of vacancies while the dislocation cores are sinks. In the bottom row of Fig. 12, we observe that the stress field generated by the dislocation dipole also reflects the presence of cavities as domains inside which the stress field is actually canceled. This naturally allows for the consideration of all elastic interactions including for instance image forces of dislocations.

4.3. Kinetics analysis

As it can be observed in Fig. 11 showing a typical example of the $R_i = f(t)$ curves obtained for one of the 100 simulations, evolution of radii versus time is quite regular over the whole time interval. For this reason the closure rate of all the cavities have been extracted by performing a linear fit of these curves between 1 and 2 seconds (as for the reference closure rate v_0). This procedure has been applied for the 1000 cavities leading to the histogram displayed in Fig. 13.

In this histogram, cavities are also discriminated according to an isolation criterion. For this, a circular region with a cutoff radius R_{cut} is defined, centered on each cavity center. The number of cavities belonging to this region is established by considering that a cavity belongs to a given region when its center is included in it. A cavity is considered as isolated if there is no any other cavity located less than R_{cut} from it. Groups of 2, 3 and 4 (or more) cavities are thus defined. This procedure is performed by using the python

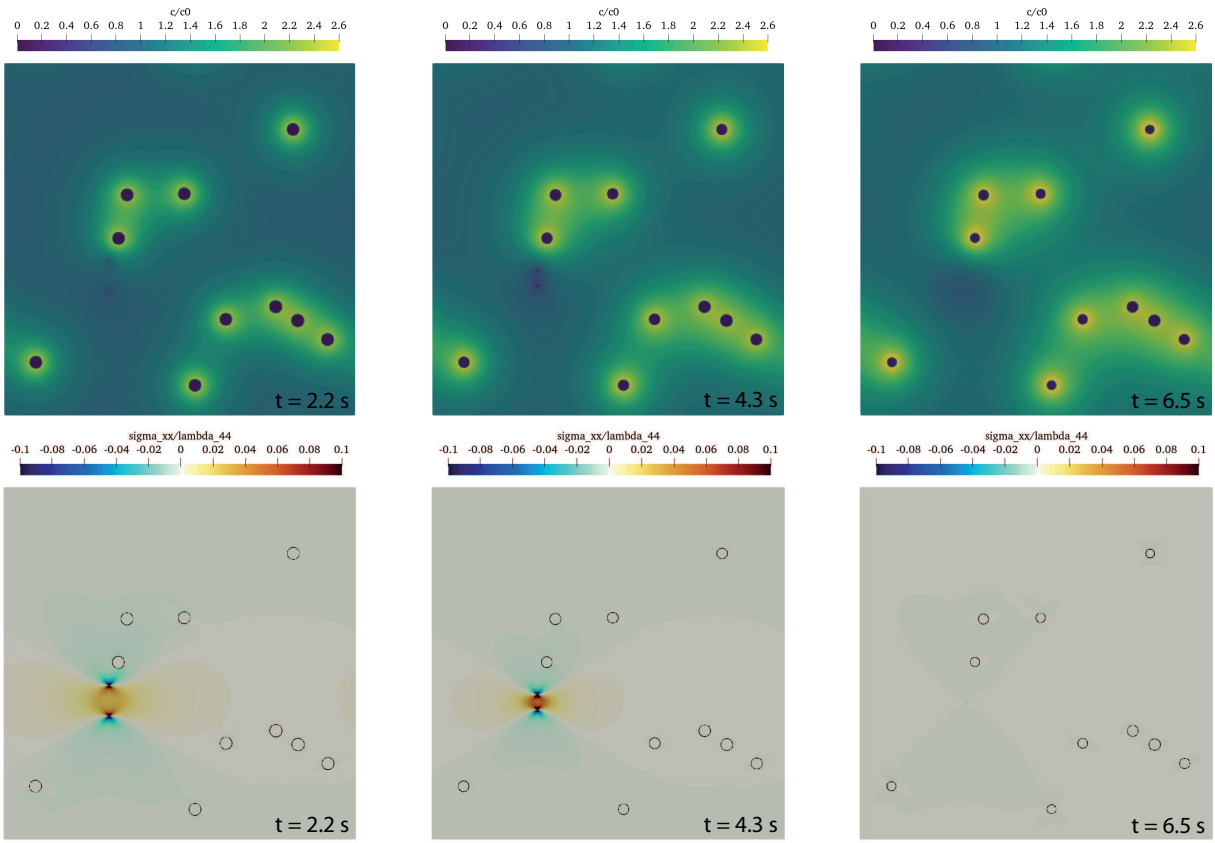

Figure 12: Microstructure evolution. (Top) Reduced vacancy concentration field c/c_0. (Bottom) Non-dimensional stress-field σ_{xx}/λ_{44}. (See colors on-line)

routine sklearn.cluster.DBSCAN 3 [84]. Here, by anticipating that the behavior of a given cavity should depend on whether its distance to its first neighbors is smaller or larger than half the overall average distance between first neighbor cavities, we fix the cutoff radius to $R_{cut} = 10$ nm which is nothing but the value used in Sec. 4.2 to compute the reference velocity v_0. In this histogram, each group is discriminated by a color. The reference velocity v_0 of an isolated cavity is also reported.

In Fig. 13, two main peaks can be observed indicating that cavities are globally separated in two groups of closure rate. The main group is represented by the highest peak that indicates an average closure rate of about 0.10 nm/s, while peak of the second less represented group indicates a lower rate of about 0.07 nm/s. With the isolation criterion introduced above, it is straightforward to see that cavities considered as isolated (in blue) compose the main peak while the others (orange, green, red) compose the second peak associated to the lower closure rate. This reveals that the more cavities are clustered the slower the closure. In Fig. 12, this phenomenon is visible on the concentration map at $t = 6.5$ s where it can be noticed that an isolated cavity is smaller than clustered cavities.

This result is due to a screening effect of the diffusion field that can be understood qualitatively by remembering that the closure rate of cavities depends on the vacancy flux. At the lowest order, this flux is proportional to the gradient of vacancy concentrations. This gradient is roughly given by the supersaturation of vacancies close to cavities induced by the Gibbs-Thomson effect and the distance to other sinks. When a cavity is surrounded by other cavities, similar concentrations imposed by the Gibbs-Thomson effect of nearby cavities are present, which tends to decrease the gradients, and so the fluxes.

This result can even be quantified analytically by following the elegant approach introduced in [57]. The principle is to consider the Green functions of diffusion by assuming in particular that cavities remain circular during their closure (which is widely verified in our simulations). The closure rate of a given cavity i surrounded

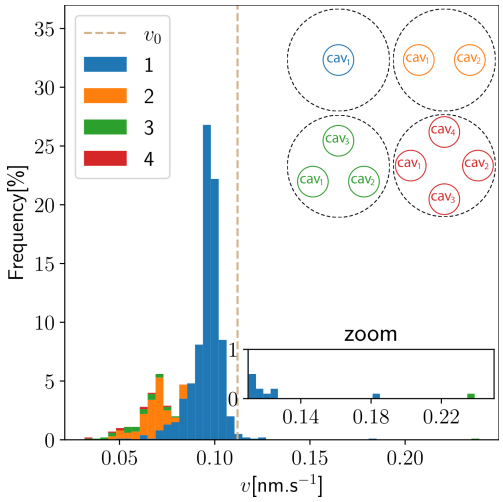

Figure 13: Histogram showing the percentage of cavity as a function of their closure rate v at t = 2 s. The reference closure rate v_0 is indicated by the dotted line. Bars are colored according to the isolation criterion: blue = 1 cavity ; orange = 2 cavities; green = 3 cavities; red = 4 cavities. (See colors on-line)

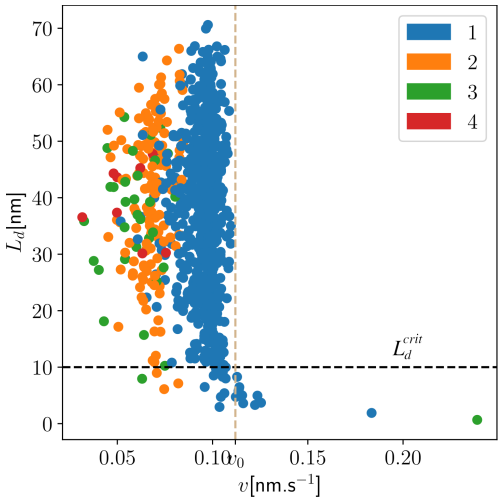

Figure 14: Cavity-dislocation distance L_d versus cavity closure rate v. The reference closure rate v_0 is indicated by the dotted line. Points are colored according to the isolation criterion. (See colors on-line)

by N cavities can be established formally (see Eq. (97) of [57] for the 3D result with two cavities). By following a similar reasoning in 2D, one gets:

$$\frac{\mathrm{d}R_i}{\mathrm{d}t} = \frac{1}{R_i \ln\left(R_i/R_\infty\right)}\left[D_v\left(c_i^+ - c_0\right) - \sum_{\substack{j=1 \\ j\neq i}}^{N} R_j \ln\left(\frac{r_{ij}}{R_\infty}\right)\frac{\mathrm{d}R_j}{\mathrm{d}t}\right], \tag{58}$$

where D_v is the vacancy diffusivity, c_i^+ the vacancy concentration in the matrix side of the i^{th} cavity surface, r_{ij} the distance separating cavities i and j, and $R_\infty \gg R_i$ the external radius of the system assumed to be circular. By assuming that all cavities collapse and by noting the closure rate of the i^{th} cavity $v_i = \mathrm{d}R_i/\mathrm{d}t$ and that of the same cavity in the absence of others v_i^0, the previous equation can be rewritten as:

$$v_i = v_i^0 - \sum_{\substack{j=1 \\ j\neq i}}^{N} \frac{R_j \ln\left(\frac{r_{ij}}{R_\infty}\right)}{R_i \ln\left(\frac{R_i}{R_\infty}\right)} v_j. \tag{59}$$

This formula shows more quantitatively that the more cavity i is surrounded by other cavities, the more its closure rate decreases compared to the case when it is isolated. Moreover, the smaller the distance between cavities, the stronger the slowing down. Here, it is interesting to show that the phase-field description naturally accounts for this phenomenon with the added benefit of having access to the local diffusion field and potentially more complex cavity shapes.

In the histogram Fig. 13, while the majority of cavities presents a closure rate smaller than the reference one v_0, some of them are observed to collapse much faster. These cavities are actually those localized close to the dislocation dipole. This can be appreciated by plotting the distance of cavities to the dislocation dipole L_d with respect to their closure rate such as shown in Fig. 14. In this figure, the two populations of cavities (isolated or not) are also visible. We can see that it is possible to have a competition between the dipole-induced closure acceleration and the slowing down induced by cavity clustering. However, it clearly appears a distance of about $L_d^{crit} = 10$ nm below which closure rates are shifted to higher values due to the presence of the dislocation dipole. This distance appears here to be characteristics of the diffusion field. In this case, dislocation cores act as sinks for vacancies (see Fig. 12), increasing fluxes in vicinity of the closest cavities. When these former are localized below 10 nm, higher closure rate can thus be measured. This suggests that beyond this distance, the diffusion field around cavities does not seem to be affected.

All these results indicate that, in our simulations, the distance of 10 nm is characteristic of the quasi-static diffusion field for a reason that is ultimately only geometric, since it corresponds to about half the average distance separating a cavity from its first neighbors. Below this distance, the diffusion field is sufficiently perturbed for the closure of a cavity to be slowed or accelerated, depending on whether the neighboring object acts as a source or a sink of vacancies. Beyond this distance, a

cavity behaves like an isolated cavity.

4.4. Role of the dislocation-induced elastic interactions

In the previous subsection, it is shown how the closure kinetics of both cavities and dislocations can be affected when they are close to each other. All these results are, at least qualitatively, explainable by looking at the way diffusion field may be affected by the relative position of objects. There is however a result which has not been commented yet: even though a cavity can be considered as isolated (blue peak in Fig. 13), its closure rate is below the reference value v_0.

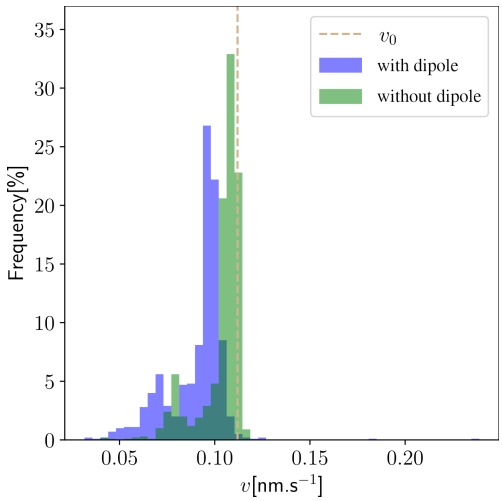

Figure 15: Histogram showing the percentage of cavity as a function of their closure rate v with and without the dislocation dipole. (See colors on-line)

To explain this, one has to account for the elastic interactions. Indeed, as shown in Fig. 12, the dislocation dipole generates an elastic field that contributes the total energy variation of the system. To evaluate its influence on the global closure kinetics of cavities, the 100 simulations performed previously have been run again without the dislocation dipole. The histogram obtained in this case is reported in Fig. 15 where it is compared to the histogram provided in Fig. 13. This figure immediately shows that all the closure rates are shifted to higher values when dislocations are removed. In particular, the main peak still related to cavities that can considered as isolated is placed around the reference closure rate v_0 as expected. This figure shows clearly that the dislocation dipole induces a decrease of the closure rate of all the cavities. From a purely diffusive point of view, this result may appear as counter-intuitive since it has been previously shown that dislocations are vacancies sinks which are likely to accelerate the cavity closure.

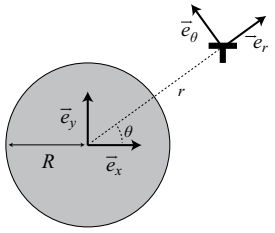

Figure 16: 2D scheme of a single cavity interacting with one edge dislocation.

Numerically, it can be verified that elastic energy contributions to the total energy variation of the system explain this difference in the closure kinetics. Formally, such a result can also be streamlined by considering the simplest 2D case of a single cavity interacting with one edge dislocation such as shown in Fig. 16. In this case, by considering a plane strain state and an elastically isotropic material, there is an analytical result describing the elastic interaction between these objects. This solution provided in [85, 86] writes:

$$\Delta E^{el}_{int} = -\frac{\mu b^2}{4\pi\,(1-\nu)}\left[\frac{R^2}{r^2}\cos^2\theta + \ln\left(\frac{r^2}{r^2-R^2}\right)\right], \quad (60)$$

where μ is the shear modulus and b the Burgers vector. To evaluate the impact of the dislocation on cavity closure, this expression is derived with respect to the cavity radius R:

$$\frac{\partial \Delta E^{el}_{int}}{\partial R} = -\frac{\mu b^2}{4\pi\,(1-\nu)}\,2R\left(\frac{1}{r^2} + \frac{\cos^2\theta}{r^2-R^2}\right). \quad (61)$$

Since $r \geq R$, this derivative is always negative: this means that a variation $\mathrm{d}R < 0$ of cavity closure will always cause an unfavorable increase of the elastic interaction energy. Hence, these interactions are expected to systematically slow down the cavity closure, except if the dipole is significantly far away from the cavities (ΔE^{el}_{int} drops to zero when $r \to +\infty$) or its own closure kinetics is so fast that such a phenomenon cannot be appreciated. Under these conditions, elastic interactions can be neglected in the kinetic analysis. Otherwise, the phase-field simulations show that it is significant.

With the current results, we can anticipate that in the presence of a high cavity density, the elastic fields generated by the dislocation are likely to be screened by the cavities located in the immediate environment of the dipole. As a possible consequence, impact of the elastic field on the kinetics of the more distant cavities could be reduced so that the slowdown of the average shrinkage rate of all the cavities is less pronounced. Conversely, a high density of dislocations may exacerbate this effect unless their stress field is mutually screened. Of

course, establishing a more quantitative link between the shrinkage rate of all cavities and the respective density of the two classes of objects would require a specific study that goes beyond the scope of this study, which focuses primarily on the development of the model and its potential, but which could be addressed in future works. In these studies, 3D cases in which the elastic effects are different could also be considered, as well as taking into account mechanisms that have not yet been introduced in the modeling, such as high gas pressure inside the cavities or the presence of other defects in the system (grain boundaries, etc.).

5. Conclusion

In the first part of this work, an original phase-field formalism is proposed to couple cavity growth, dislocation climb and vacancy diffusion. This model is based on a variational formalism and kinetics guaranteeing that matter is conserved during the diffusion processes while the elastic interactions are naturally accounted for. Details of the numerical implementations of the model are also provided. In particular, a very efficient algorithm is exposed to solve $\dot{c} = 0$ using a spectral method and a fixed point algorithm. It is subsequently shown how this method allows us to significantly accelerate the simulation of diffusion-controlled processes by a factor 1000 at least compared to a case in which $\dot{c}$ is explicitly integrated. Then, simulations of the cavity closure and dislocation climb in simple geometries are performed in order to demonstrate ability of the modeling to quantitatively reproduce diffusion-controlled processes. The comparison between simulation results and the theoretical analysis also allows us to select all parameters of the model in a physically justified way.

In the last part, the microstructure evolution of an annealed aluminum sample (ten cavities and one interstitial dislocation dipole in a $102.4\,nm \times 102.4\,nm$ system) is studied as a direct application of the model. Several interesting results are found and explained: (i) the closure rate of clustered cavities decreases due to the interaction of their mutual vacancy diffusion fields; (ii) the dislocation dipole acts as a sink for vacancies that accelerates the closure rate of very close cavities; (iii) long range elastic interactions are however shown to slow down the average closure rate of all the cavities. This study shows that our method is particularly promising to quantify and explain the evaporation kinetics of cavities and dislocations in annealed irradiated materials.

One natural perspective for this work would be to envisage a direct confrontation between simulations and experiments on the evaporation kinetics of cavities. For this, it might be advisable to perform specific model experiments where we could modify the respective densities of the two classes of objects by changing the experimental irradiation conditions (flux, temperature...). In this case, one should be able to quantify the shrinkage kinetics of cavity with respect to these densities and directly compared the results with corresponding simulations. The interest of such a specific approach is that even though the simulations do not contain all the physics involved in real systems, the main tendencies could be compared and be sufficient to conclude on the impact of elasticity. To go beyond this work, it would also be advisable to simulate 3D full field cases where the diffusion field spatially decays in $1/r$ instead of $\ln(r)$ around cavities. In the context of irradiated materials, the model could be enriched by integrating: interstitial diffusion and its coupling with the other fields [22, 23, 27, 29, 30, 31], grain boundaries [17, 19, 28, 33] and/or the presence of a gas pressure inside cavities [20, 18, 21, 24, 32]. Anisotropic surface energy and/or surface stresses might also be considered to account for faceting [25, 26, 13].

The present model could finally be used in other contexts where a diffusion-mediated interplay between cavities and dislocations also occurs. As an example, we recently studied the role of plastic activity on micro-pore closure kinetics in nickel-based super-alloys placed under Hot Isostatic Pressure (HIP) [87]. In this work, only gliding dislocations were considered and interesting equilibrium configuration of loops around a pore were identified under an external applied pressure. These final configurations could be used as initial ones for the climb which is known to be a slower process. Such a study would help us to quantify the significance of climb processes in the multi-physics HIP pore closure kinetics [88].

Data availability

The raw/processed data required to reproduce these findings can be provided by the authors on reasonable request.

Appendix A. Asymptotic analysis of the phase-field equations for the cavity shrinkage

Appendix A.1. System, equations and generic solutions for η and μ

We consider the system described in Fig. 3 which is a cylindrical (in 2D) or spherical (in 3D) cavity of radius

R, embedded in a matrix where the vacancy concentration is fixed at $c_\infty < c_0$ on an external cylinder (in 2D) or a sphere (in 3D) of radius $R_\infty > R$. In this calculation, elastic effects are neglected. Symmetries of the problem also impose radial solutions for the fields η and c which thus only depend on the radial coordinate r. In this case, evolution of the cavity is described by Eqs. (25) and (27) that are rewritten here as:

$$\dot{\eta} = -L_\eta \left[\frac{\partial f_{cav}^{homo}}{\partial \eta} - \frac{3}{2}\gamma\xi \left(\frac{\partial^2 \eta}{\partial r^2} + \frac{(D-1)}{r}\frac{\partial \eta}{\partial r} \right) + \frac{\partial f_{chem}}{\partial \eta} - \mu \right], \tag{A.1}$$

$$0 = M\nabla^2\mu - \dot{\eta}, \tag{A.2}$$

where D is the space dimension and μ is the chemical potential linked to the concentration field c by Eq. (10):

$$\mu = \frac{\partial f_{chem}}{\partial c} = \frac{k_B T}{\Omega c_0}\Big[(\mathcal{K}-1)h(\eta)+1\Big]\Big[c - c_0(1-h(\eta))\Big]. \tag{A.3}$$

In the absence of coupling with any other fields, when $R \to +\infty$, one can consider that the phase-field η accounts for a static diffuse plane surface at $r = R$ which is the solution of:

$$\frac{\partial f_{cav}^{homo}}{\partial \eta} - \frac{3}{2}\gamma\xi\frac{\partial^2 \eta}{\partial r^2} = 0. \tag{A.4}$$

When $\eta(r=0) \to 1$ and $\eta(r \to +\infty) = 0$, one obtains the following equilibrium profile:

$$\eta_{eq}(r) = \frac{1}{2}\left(1 + \tanh\left(\frac{2(R-r)}{\xi}\right)\right). \tag{A.5}$$

It is then postulated that this solution still applies when η is coupled to other fields and describes a moderately curved surface evolving with time. Under these conditions, Eqs. (A.1) and (A.2) become:

$$-v\frac{\partial \eta_{eq}}{\partial r} = -L_\eta\left(-\frac{3}{2}\gamma\xi\frac{(D-1)}{r}\frac{\partial \eta_{eq}}{\partial r} + \frac{\partial f_{chem}}{\partial \eta_{eq}} - \mu\right), \tag{A.6}$$

$$0 = M\nabla^2\mu + v\frac{\partial \eta_{eq}}{\partial r}, \tag{A.7}$$

where $v = \mathrm{d}R/\mathrm{d}t$ is the radial velocity of the interface.

Outside the diffuse surface, $\partial\eta_{eq}/\partial r = 0$ such that μ can be calculated with Eq. (A.7) that reduces to the Laplace's equation $\nabla^2\mu = 0$. In 2D, this leads to:

$$\begin{aligned} r \le R &: \ \mu(r) = \mu_{surf}, \\ r > R &: \ \mu(r) = \mu_\infty + \left(\mu_\infty - \mu_{surf}\right)\frac{\ln(r/R_\infty)}{\ln(R_\infty/R)}, \end{aligned} \tag{A.8}$$

and in 3D:

$$\begin{aligned} r \le R &: \ \mu(r) = \mu_{surf}, \\ r > R &: \ \mu(r) = \mu_\infty + \left(\mu_\infty - \mu_{surf}\right)\frac{R}{R_\infty - R}\left(1 - \frac{R_\infty}{r}\right). \end{aligned} \tag{A.9}$$

μ is supposed to be continuous in the diffuse surface region (where $\partial\eta_{eq}/\partial r \neq 0$) and given by $\mu = \mu_{surf}$ which is unknown yet. μ_∞ corresponds to the chemical potential at R_∞ and is given by $\mu_\infty = k_B T\left(c_\infty - c_0\right)/\left(\Omega c_0\right)$ according to Eq. (A.3) when $\eta = 0$. It is an input of the problem.

Appendix A.2. Calculation of μ_{surf} and v

μ_{surf} is determined with the help of Eq. (A.6) evaluated in the surface domain by multiplying it by $\partial\eta_{eq}/\partial r$ and by integrating it over the domain which is formally bounded by sign "−" (cavity side) and sign "+" (matrix side):

$$\begin{aligned} v\int_-^+ \left(\frac{\partial \eta_{eq}}{\partial r}\right)^2 \mathrm{d}r = L_\eta\Bigg(&-\frac{3}{2}\gamma\xi\int_-^+ \frac{(D-1)}{r}\left(\frac{\partial \eta_{eq}}{\partial r}\right)^2 \mathrm{d}r \\ &+ \int_-^+ \frac{\partial f_{chem}}{\partial r}\mathrm{d}r - \int_-^+ \mu\frac{\partial \eta_{eq}}{\partial r}\mathrm{d}r\Bigg). \end{aligned} \tag{A.10}$$

In practice, μ and $(D-1)/r$ slightly vary within the surface domain with respect to $\partial\eta_{eq}/\partial r$ and can thus be taken equal to μ_{surf} and $(D-1)/R$, respectively. Furthermore, one can show that $\int_-^+ \left(\partial\eta_{eq}/\partial r\right)^2 \mathrm{d}r = 2/(3\xi)$ by construction of the phase-field model [2]. This leads to:

$$\frac{2v}{3\xi L_\eta} = -\frac{(D-1)}{R}\gamma + \Delta f_{chem}^{surf} - \mu_{surf}\Delta\eta_{eq}^{surf}, \tag{A.11}$$

$$\frac{2v}{3\xi L_\eta} = -\frac{(D-1)}{R}\gamma + \Delta f_{chem}^{surf} + \mu_{surf}, \tag{A.12}$$

with $\Delta f_{chem}^{surf} = f_{chem}^{+} - f_{chem}^{-}$ et $\Delta\eta_{eq}^{surf} = \eta_{eq}^{+} - \eta_{eq}^{-} = -1$ by definition. We also have:

$$\mu = \frac{\partial f_{chem}}{\partial c}, \tag{A.13}$$

$$\int_-^+ \mu\frac{\partial c}{\partial r}\mathrm{d}r = \int_-^+ \frac{\partial f_{chem}}{\partial r}\mathrm{d}r, \tag{A.14}$$

$$\mu_{surf}\Delta c^{surf} = \Delta f_{chem}^{surf}, \tag{A.15}$$

[2] One may take 0 as the lower bound and $+\infty$ as the upper bound for all terms of integrals.

with $\Delta c^{surf} = c^+ - c^-$. By putting this result in Eq. (A.12), one obtains:

$$\mu_{surf} = \frac{\frac{2v}{3\xi L_\eta} + \frac{(D-1)}{R}\gamma}{\Delta c^{surf} + 1}. \tag{A.16}$$

The surface concentration jump Δc^{surf} is estimated by assuming that the vacancy concentration near the surface is very close to the expected equilibrium value: $\Delta c^{surf} = c^+ - c^- = c_0$. Furthermore, the equilibrium concentration of vacancy in the matrix c_0 is generally very low such that $c_0 \ll 1$. This allows us to finally write:

$$\mu_{surf} = \frac{2v}{3\xi L_\eta} + \frac{(D-1)}{R}\gamma. \tag{A.17}$$

In this equation, μ_{surf} is expressed as a function of the radial velocity of the cavity v that can also be evaluated by starting from Eq. (A.7) integrated over the diffuse surface domain:

$$0 = M\int_-^+ \nabla^2\mu \mathrm{d}r + v\int_-^+ \frac{\partial \eta_{eq}}{\partial r}\mathrm{d}r, \tag{A.18}$$

$$0 = M\left[\left(\frac{\partial \mu}{\partial r}\right)^+ - \left(\frac{\partial \mu}{\partial r}\right)^-\right] + v\Delta\eta_{eq}^{surf}, \tag{A.19}$$

$$v = M\left[\left(\frac{\partial \mu}{\partial r}\right)^+ - \left(\frac{\partial \mu}{\partial r}\right)^-\right]. \tag{A.20}$$

By using the solutions of μ given Eqs. (A.8) and (A.9), one gets:

$$\left(\frac{\partial \mu}{\partial r}\right)^- = 0, \tag{A.21}$$

$$\left(\frac{\partial \mu}{\partial r}\right)^+ = \frac{\mu_\infty - \mu_{surf}}{\rho_D^\infty(R)}, \tag{A.22}$$

where ρ_D^∞ is a function of the cavity radius R that depends on the space dimension D and the value R_∞. It is such that $\rho_2^\infty(R) = R\ln(R_\infty/R)$ and $\rho_3^\infty(R) = R(1 - R/R_\infty)$. This allows us to calculate:

$$v = M\frac{\mu_\infty - \mu_{surf}}{\rho_D^\infty(R)}. \tag{A.23}$$

By putting Eq. (A.17) in the previous equations, one finally gets on expression of the radial velocity that writes:

$$v = \frac{-D_v(c_0 - c_\infty) - M\frac{(D-1)\gamma}{R}}{\rho_D^\infty(R) + 2M/\left(3\xi L_\eta\right)}. \tag{A.24}$$

It is worth recalling that D_v is the vacancy diffusivity defined with Eq. (24). One can also establish another expression of the surface chemical potential that writes:

$$\mu_{surf} = \frac{\frac{(D-1)\gamma}{R} + \frac{2M/\left(3\xi L_\eta\right)}{\rho_D^\infty(R)}\mu_\infty}{1 + \frac{2M/\left(3\xi L_\eta\right)}{\rho_D^\infty(R)}}. \tag{A.25}$$

Appendix A.3. Comments on the 3D asymptotic kinetic regimes

In Sec. 3, it is shown that working under the local equilibrium assumption is equivalent to consider $L_\eta \to +\infty$. In 3D, this hypothesis lead to the surface chemical potential $\mu_{surf} = 2\gamma/R$. By considering that μ inside the cavity is given by Eq. (A.3) when $\eta = 1$, while outside it is given by Eq. (A.3) when $\eta = 0$, one can show that the 3D concentration profile is:

$$\begin{aligned} r \le R \;&:\; c(r) = c^-, \\ r > R \;&:\; c(r) = c_\infty + (c_\infty - c^+)\frac{R}{R_\infty - R}\left(1 - \frac{R_\infty}{r}\right). \end{aligned} \tag{A.26}$$

where c^- and c^+ are the concentrations on both sides of the surface given by $c^- = 2d_0/(\mathcal{K}R)$ and $c^+ = c_0 + 2d_0/R$ with the capillary length d_0 defined by: $d_0 = \Omega c_0\gamma/(k_BT)$.

Now, if we consider a realistic experimental context where $R_\infty \gg R$ is postulated, then Eq. (46) can be simplified as follows:

$$v = 2D_v\frac{d_0}{R}\left(\frac{1}{\overline{R_c}} - \frac{1}{R}\right), \tag{A.27}$$

with the algebraic critical radius $\overline{R_c}$ defined by:

$$\overline{R_c} = \frac{2d_0}{c_\infty - c_0}. \tag{A.28}$$

This radius distinguishes a kinetic regime controlled by the marginal relaxation of energy related to the redistribution of vacancies by diffusion (case where $R \gg \left|\overline{R_c}\right|$) from the regime where this relaxation is linked to the decrease in surface energy (case where $R \ll \left|\overline{R_c}\right|$) [57]. We show in particular that when $R \gg \left|\overline{R_c}\right|$, the integration of $v = \mathrm{d}R/\mathrm{d}t$ gives the following evolution law of the cavity radius [88]:

$$R^2(t) = R_0^2 - D_v(c_0 - c_\infty)t, \tag{A.29}$$

while, when $R \ll \left|\overline{R_c}\right|$, we have:

$$R^3(t) = R_0^3 - 6M\gamma t. \tag{A.30}$$

When $c_\infty < c_0$, these laws both predict a decrease of the cavity radius, asymptotically in square or cubic root of time following that R is much larger or much smaller than $R_c = 2d_0/(c_0 - c_\infty)$. The vacancy concentration profile given Eq. (A.26) can be rewritten according to this critical radius as:

$$\begin{aligned} r \le R \;\; &: \;\; c(r) = \frac{2d_0}{\mathcal{K}R}, \\ r > R \;\; &: \;\; c(r) = c_\infty + 2\left(1 - \frac{R}{R_c}\right)\frac{d_0}{r}. \end{aligned} \tag{A.31}$$

Appendix B. Asymptotic analysis of the phase-field equations for the dislocation climb

Appendix B.1. System, equations and generic solutions for ϕ and μ

We reconsider here the system described in Fig. 6 by focusing only on the top dislocation. For the formal analysis, we consider that its core remains centered in a 2D matrix where the vacancy concentration is fixed at c_∞ on a cylinder of radius R_∞, even during its stationary movement. The core region of the dislocation is defined by a disc of radius $r_0 \ll R_\infty$. A constant applied stress σ^A_{ij} is considered such that $\sigma^A_{ij} = \sigma^A_{11}\overrightarrow{e}_x \otimes \overrightarrow{e}_x$. The dislocation phase-field is confined in the $x = 0$ plane and just depends on the y coordinate in the Cartesian frame. For symmetrical reasons, fields μ and c depend on the radial coordinate r in the polar frame. In this case, Eqs. (26) and (27) explicitly write:

$$\dot{\phi} = -L_\phi\left[\frac{\partial f^{homo}_{disl}}{\partial \phi} - \frac{\pi}{2}\Gamma w\frac{\partial^2\phi}{\partial y^2} + \sigma_{11}bh'(\phi) - b\mu\Big|_{\theta=\pi/2}\right], \tag{B.1}$$

$$0 = M\nabla^2\mu - b\dot{\phi}\delta(x), \tag{B.2}$$

where μ is the chemical potential linked to the concentration field c by:

$$\mu = \frac{\partial f_{chem}}{\partial c} = \frac{k_BT}{\Omega c_0}\big(c - c_0\big), \tag{B.3}$$

according to Eq. (10) when $\eta = 0$ (no cavity).

In the absence of applied stresses, at chemical equilibrium, the phase-field ϕ accounts for a static diffuse core at $y = 0$ which is the solution of:

$$\frac{\partial f^{homo}_{disl}}{\partial \phi} - \frac{\pi}{2}\Gamma w\frac{\partial^2\phi}{\partial y^2} + \sigma^{disl}_{11}bh'(\phi) = 0, \tag{B.4}$$

where σ^{disl}_{11} is the stress field generated by the dislocation itself. Usually, it is assumed that σ^{disl}_{11} is small, such that the profile is correctly described by:

$$\frac{\partial f^{homo}_{disl}}{\partial \phi} - \frac{\pi}{2}\Gamma w\frac{\partial^2\phi}{\partial y^2} = 0. \tag{B.5}$$

When $\phi(y \to -\infty) \to 1$ and $\phi(y \to +\infty) = 0$, the equilibrium profile is given by:

$$\phi_{eq}(y) = 1 - \frac{2}{\pi}\arctan\left(\exp\left(\frac{\pi y}{w}\right)\right). \tag{B.6}$$

When a constant additional stress $\sigma^A_{11} \neq 0$ is applied and $\mu \neq 0$, the dislocation is assumed to reach a stationary state by climbing at a constant velocity v. By postulating that the equilibrium solution still applies at stationary state, one has $\phi \approx \phi_{eq}(y + vt)$ and Eqs. (B.1) and (B.2) become:

$$v\frac{\partial \phi_{eq}}{\partial y} = L_\phi b\left(\sigma^A_{11}h'(\phi_{eq}) - \mu\Big|_{\theta=\pi/2}\right), \tag{B.7}$$

$$0 = M\nabla^2\mu + v\frac{\partial \phi_{eq}}{\partial y}\delta(x). \tag{B.8}$$

Outside the core region, $\partial\phi_{eq}/\partial y = 0$ in Eq. (B.8) and μ is solution of the Laplace's equation $\nabla^2\mu = 0$ that gives:

$$\mu(r) = \mu_\infty + (\mu_\infty - \mu_{core})\frac{\ln(r/R_\infty)}{\ln(R_\infty/r_0)}, \tag{B.9}$$

where μ_{core} is the chemical potential in the dislocation core which is unknown yet. As for the cavity, $\mu_\infty = k_BT(c_\infty - c_0)/(\Omega c_0)$ corresponds to the chemical potential at R_∞ imposed by the value of c_∞.

Appendix B.2. Calculation of μ_{core} and v

μ_{core} can be evaluated by multiplying Eq. (B.7) with $\partial\phi_{eq}/\partial y$ and by integrating it over the core domain:

$$\begin{aligned} v\int_{-r_0}^{+r_0}\left(\frac{\partial \phi_{eq}}{\partial y}\right)^2 \mathrm{d}y = L_\phi b\Bigg(&\sigma^A_{11}\int_{-r_0}^{+r_0} h'(\phi_{eq})\frac{\partial \phi_{eq}}{\partial y}\mathrm{d}y \\ &- \int_{-r_0}^{+r_0}\mu\Big|_{\theta=\pi/2}\frac{\partial \phi_{eq}}{\partial y}\mathrm{d}y\Bigg) \end{aligned} \tag{B.10}$$

In the core region, $\mu\big|_{\theta=\pi/2} = \mu_{core}$ which is assumed to marginally vary with respect to $\partial\phi_{eq}/\partial y$. Furthermore, one can show that $\int_{-r_0}^{+r_0}\left(\partial\phi_{eq}/\partial y\right)^2 \mathrm{d}y = 2/(\pi w)$ by construction of the phase-field model [3]. Thus, calculation of the integrals becomes straightforward, leading to:

$$\mu_{core} = \sigma^A_{11} - \frac{2v}{\pi w L_\phi b}. \tag{B.11}$$

[3] Integral bounds are taken at infinity to simplify the calculations.

μ_{core} is expressed as a function of the dislocation velocity v that can also be evaluated by starting from Eq. (B.8) integrated over the core domain:

$$0 = 2\pi M \int_0^{r_0} \left(\nabla^2 \mu\right) r \mathrm{d}r + vb \int_{-r_0}^{+r_0} \frac{\partial \phi_{eq}}{\partial y} \mathrm{d}y, \quad \text{(B.12)}$$

$$0 = 2\pi M r_0 \left(\frac{\partial \mu}{\partial r}\right)_{r=r_0} - vb. \quad \text{(B.13)}$$

By using the solutions of μ given Eq. (B.9), one obtains:

$$v = \frac{2\pi M}{b \ln\left(R_\infty / r_0\right)} \left(\mu_\infty - \mu_{core}\right). \quad \text{(B.14)}$$

By putting Eq. (B.11) in the previous equations, one finally gets on expression of the climb velocity that can be written as:

$$v = \frac{\frac{2\pi D_v c_0}{b} \left(\frac{c_\infty}{c_0} - 1 - \frac{\Omega \sigma_{11}^A}{k_B T}\right)}{\ln\left(R_\infty / r_0\right) + \frac{4M}{w L_\phi b^2}}, \quad \text{(B.15)}$$

where D_v is the vacancy diffusivity given Eq. (24). One can also establish another expression of the core chemical potential that writes:

$$\mu_{core} = \frac{\sigma_{11}^A + \frac{4M\mu_\infty}{w L_\phi b^2 \ln(R_\infty / r_0)}}{1 + \frac{4M}{w L_\phi b^2 \ln(R_\infty / r_0)}}. \quad \text{(B.16)}$$

References

[1] N. Moelans, B. Blanpain, P. Wollants, An introduction to phase-field modeling of microstructure evolution, Calphad 32 (2) (2008) 268–294.

[2] I. Steinbach, Phase-field models in materials science, Modelling and simulation in materials science and engineering 17 (7) (2009) 073001.

[3] Y. Li, S. Hu, X. Sun, M. Stan, A review: applications of the phase field method in predicting microstructure and property evolution of irradiated nuclear materials, npj Computational Materials 3 (1) (2017) 16.

[4] P. C. Hohenberg, B. I. Halperin, Theory of dynamic critical phenomena, Reviews of Modern Physics 49 (3) (1977) 435.

[5] H.-C. Yu, W. Lu, Dynamics of the self-assembly of nanovoids and nanobubbles in solids, Acta Materialia 53 (6) (2005) 1799–1807.

[6] S. Hu, C. H. Henager Jr, Phase-field modeling of void lattice formation under irradiation, Journal of Nuclear Materials 394 (2-3) (2009) 155–159.

[7] Y. Li, S. Hu, X. Sun, F. Gao, C. H. Henager Jr, M. Khaleel, Phase-field modeling of void migration and growth kinetics in materials under irradiation and temperature field, Journal of Nuclear Materials 407 (2) (2010) 119–125.

[8] A. Semenov, C. Woo, Interfacial energy in phase-field emulation of void nucleation and growth, Journal of nuclear materials 411 (1-3) (2011) 144–149.

[9] A. Semenov, C. Woo, Phase-field modeling of void formation and growth under irradiation, Acta materialia 60 (17) (2012) 6112–6119.

[10] Z. Xiao, A. Semenov, C. Woo, S.-Q. Shi, Single void dynamics in phase field modeling, Journal of nuclear materials 439 (1-3) (2013) 25–32.

[11] X. Ding, J. Zhao, H. Huang, S. Ding, Y. Huo, Effect of damage rate on the kinetics of void nucleation and growth by phase field modeling for materials under irradiations, Journal of Nuclear Materials 480 (2016) 120–128.

[12] Y. Gao, Y. Zhang, D. Schwen, C. Jiang, C. Sun, J. Gan, Formation and self-organization of void superlattices under irradiation: A phase field study, Materialia 1 (2018) 78–88.

[13] M. Javanbakht, M. S. Ghaedi, Phase field approach for void dynamics with interface stresses at the nanoscale, International Journal of Engineering Science 154 (2020) 103279.

[14] M. Noble, M. Tonks, S. Fitzgerald, Turing instability in the solid state: Void lattices in irradiated metals, Physical review letters 124 (16) (2020) 167401.

[15] Y. Gao, A. M. Jokisaari, L. Aagesen, Y. Zhang, M. Jin, C. Jiang, S. Biswas, C. Sun, J. Gan, The effect of elastic anisotropy on the symmetry selection of irradiation-induced void superlattices in cubic metals, Computational Materials Science 206 (2022) 111252.

[16] S. Rokkam, A. El-Azab, P. Millett, D. Wolf, Phase field modeling of void nucleation and growth in irradiated metals, Modelling and simulation in materials science and engineering 17 (6) (2009) 064002.

[17] P. C. Millett, S. Rokkam, A. El-Azab, M. Tonks, D. Wolf, Void nucleation and growth in irradiated polycrystalline metals: a phase-field model, Modelling and simulation in materials science and engineering 17 (6) (2009) 064003.

[18] P. C. Millett, M. Tonks, Application of phase-field modeling to irradiation effects in materials, Current Opinion in Solid State and Materials Science 15 (3) (2011) 125–133.

[19] P. C. Millett, A. El-Azab, S. Rokkam, M. Tonks, D. Wolf, Phase-field simulation of irradiated metals: Part i: Void kinetics, Computational materials science 50 (3) (2011) 949–959.

[20] P. C. Millett, A. El-Azab, D. Wolf, Phase-field simulation of irradiated metals: Part ii: Gas bubble kinetics, Computational Materials Science 50 (3) (2011) 960–970.

[21] Y. Li, S. Hu, R. Montgomery, F. Gao, X. Sun, Phase-field simulations of intragranular fission gas bubble evolution in uo2 under post-irradiation thermal annealing, Nuclear Instruments and Methods in Physics Research Section B: Beam Interactions with Materials and Atoms 303 (2013) 62–67.

[22] A. El-Azab, K. Ahmed, S. Rokkam, T. Hochrainer, Diffuse interface modeling of void growth in irradiated materials. mathematical, thermodynamic and atomistic perspectives, Current opinion in solid state and materials science 18 (2) (2014) 90–98.

[23] N. Wang, S. Rokkam, T. Hochrainer, M. Pernice, A. El-Azab, Asymptotic and uncertainty analyses of a phase field model for void formation under irradiation, Computational materials science 89 (2014) 165–175.

[24] S. Hu, D. E. Burkes, C. A. Lavender, D. J. Senor, W. Setyawan, Z. Xu, Formation mechanism of gas bubble superlattice in umo metal fuels: Phase-field modeling investigation, Journal of Nuclear Materials 479 (2016) 202–215.

[25] W. Liu, N. Wang, Y. Ji, P. Song, C. Zhang, Z. Yang, L. Chen, Effects of surface energy anisotropy on void evolution during irradiation: A phase-field model, Journal of Nuclear Materials 479 (2016) 316–322.

[26] G. Han, H. Wang, D.-Y. Lin, X. Zhu, S. Hu, H. Song, Phase-field modeling of void anisotropic growth behavior in irradiated

zirconium, Computational Materials Science 133 (2017) 22–34.
[27] M. R. Tonks, A. Cheniour, L. Aagesen, How to apply the phase field method to model radiation damage, Computational Materials Science 147 (2018) 353–362.
[28] H. Wang, S. Biswas, Y. Han, V. Tomar, A phase field modeling based study of microstructure evolution and its influence on thermal conductivity in polycrystalline tungsten under irradiation, Computational Materials Science 150 (2018) 169–179.
[29] Y. Wang, J. Ding, Y. Chen, J. Zhao, Y. Wang, Three-dimensional phase field simulation of intragranular void formation and thermal conductivity in irradiated α-fe, Journal of materials science 53 (2018) 11002–11014.
[30] K. Ahmed, A. El-Azab, An analysis of two classes of phase field models for void growth and coarsening in irradiated crystalline solids, Materials Theory 2 (2018) 1–36.
[31] D. Schwen, S. Schunert, A. Jokisaari, Evolution of microstructures in radiation fields using a coupled binary-collision monte carlo phase field approach, Computational Materials Science 192 (2021) 110321.
[32] L. K. Aagesen, A. Jokisaari, D. Schwen, C. Jiang, A. Schneider, Y. Zhang, C. Sun, J. Gan, A phase-field model for void and gas bubble superlattice formation in irradiated solids, Computational Materials Science 215 (2022) 111772.
[33] G. Han, Phase-field modeling of interaction between void and grain boundaries and its swelling effect, AIP Advances 13 (8) (2023).
[34] K. A. Pendl, T. Hochrainer, Coupling stress fields and vacancy diffusion in phase-field models of voids as pure vacancy phase, Computational Materials Science 224 (2023) 112157.
[35] S. J. Zinkle, P. J. Maziasz, R. E. Stoller, Dose dependence of the microstructural evolution in neutron-irradiated austenitic stainless steel, J. Nucl. Mater. 206 (1993) 266.
[36] S. Hu, C. H. Henager, Y. Li, F. Gao, X. Sun, M. A. Khaleel, Evolution kinetics of interstitial loops in irradiated materials: a phase-field model, Modelling and Simulation in Materials Science and Engineering 20 (1) (2011) 015011.
[37] Y. Li, S. Hu, C. H. Henager Jr, H. Deng, F. Gao, X. Sun, M. A. Khaleel, Computer simulations of interstitial loop growth kinetics in irradiated bcc fe, Journal of nuclear materials 427 (1-3) (2012) 259–267.
[38] P.-A. Geslin, B. Appolaire, A. Finel, A phase field model for dislocation climb, Applied Physics Letters 104 (1) (2014).
[39] J. Ke, A. Boyne, Y. Wang, C. Kao, Phase field microelasticity model of dislocation climb: Methodology and applications, Acta materialia 79 (2014) 396–410.
[40] P.-A. Geslin, B. Appolaire, A. Finel, Multiscale theory of dislocation climb, Physical review letters 115 (26) (2015) 265501.
[41] P. Liu, S. Zheng, K. Chen, X. Wang, B. Yan, P. Zhang, S.-Q. Shi, Point defect sink strength of low-angle tilt grain boundaries: A phase field dislocation climb model, International Journal of Plasticity 119 (2019) 188–199.
[42] G. F. B. Moladje, L. Thuinet, C. S. Becquart, A. Legris, A phase field model for dislocation climb under irradiation: Formalism and applications to pure bcc iron and ferritic alloys, International Journal of Plasticity 134 (2020) 102810.
[43] X. Niu, Y. Xiang, X. Yan, Phase field model for self-climb of prismatic dislocation loops by vacancy pipe diffusion, International Journal of Plasticity 141 (2021) 102977.
[44] N. M. Ghoniem, Clustering theory of atomic defects, Radiat. Eff. Defects Solids 148 (1999) 269.
[45] R. E. Stoller, S. I. Golubov, C. Domain, C. S. Becquart, Mean field rate theory and object kinetic Monte Carlo: A comparison of kinetic models, J. Nucl. Mater. 382 (2008) 77.
[46] T. Jourdan, G. Bencteux, G. Adjanor, Efficient simulation of kinetics of radiation induced defects: A cluster dynamics approach, J. Nucl. Mater. 444 (2014) 298.
[47] T. Jourdan, Rate theory: Cluster dynamics, grouping methods, and best practices, Handbook of Materials Modeling: Applications: Current and Emerging Materials (2020) 2489–2501.
[48] C. Domain, C. Becquart, L. Malerba, Simulation of radiation damage in fe alloys: an object kinetic monte carlo approach, Journal of Nuclear Materials 335 (1) (2004) 121–145.
[49] A. F. Voter, Introduction to the kinetic monte carlo method, in: Radiation effects in solids, Springer, 2007, pp. 1–23.
[50] J. Balbuena, M. J. Caturla, E. Martínez, Kinetic monte carlo algorithms for nuclear materials applications, Handbook of Materials Modeling: Applications: Current and Emerging Materials (2020) 2193–2214.
[51] T. Jourdan, Object kinetic Monte Carlo modelling of irradiation microstructures with elastic interactions, Modell. Simul. Mater. Sci. Eng. 30 (2022) 085013.
[52] C. McElfresh, Y. Cui, S. L. Dudarev, G. Po, J. Marian, Discrete stochastic model of point defect-dislocation interaction for simulating dislocation climb, International Journal of Plasticity 136 (2021) 102848.
[53] B. Devincre, L. P. Kubin, Mesoscopic simulations of dislocations and plasticity, Materials Science and Engineering: A 234 (1997) 8–14.
[54] B. Bakó, I. Groma, G. Györgyi, G. Zimányi, Dislocation patterning: the role of climb in meso-scale simulations, Computational materials science 38 (1) (2006) 22–28.
[55] A. Lim, D. Srolovitz, M. Haataja, Low-angle grain boundary migration in the presence of extrinsic dislocations, Acta materialia 57 (17) (2009) 5013–5022.
[56] A. Breidi, S. Dudarev, Dislocation dynamics simulation of thermal annealing of a dislocation loop microstructure, Journal of Nuclear Materials 562 (2022) 153552.
[57] I. Rovelli, S. Dudarev, A. Sutton, Non-local model for diffusion-mediated dislocation climb and cavity growth, Journal of the Mechanics and Physics of Solids 103 (2017) 121–141.
[58] I. Rovelli, S. Dudarev, A. Sutton, Statistical model for diffusion-mediated recovery of dislocation and point-defect microstructure, Physical Review E 98 (4) (2018) 043002.
[59] D. Rodney, A. Finel, Phase field methods and dislocationss, MRS Online Proceedings Library 652 (2000) 1–6.
[60] Y. U. Wang, Y. Jin, A. Cuitino, A. Khachaturyan, Nanoscale phase field microelasticity theory of dislocations: model and 3d simulations, Acta materialia 49 (10) (2001) 1847–1857.
[61] A. Ruffini, Y. Le Bouar, A. Finel, Three-dimensional phase-field model of dislocations for a heterogeneous face-centered cubic crystal, Journal of the Mechanics and Physics of Solids 105 (2017) 95–115.
[62] S. G. Kim, W. T. Kim, T. Suzuki, Phase-field model for binary alloys, Physical review e 60 (6) (1999) 7186.
[63] S. Hu, Y. Li, Y. Zheng, L. Chen, Effect of solutes on dislocation motion—a phase-field simulation, International Journal of Plasticity 20 (3) (2004) 403–425.
[64] A. R. Denton, N. W. Ashcroft, Vegard's law, Physical review A 43 (6) (1991) 3161.
[65] J. W. Cahn, J. E. Hilliard, Free energy of a nonuniform system. i. interfacial free energy, The Journal of chemical physics 28 (2) (1958) 258–267.
[66] S. M. Allen, J. W. Cahn, A microscopic theory for antiphase boundary motion and its application to antiphase domain coarsening, Acta metallurgica 27 (6) (1979) 1085–1095.
[67] H. Moulinec, P. Suquet, A fast numerical method for computing the linear and nonlinear mechanical properties of composites, Comptes Rendus de l'Académie des sciences. Série II. Mécanique, physique, chimie, astronomie (1994).
[68] H. Moulinec, P. Suquet, A numerical method for computing

the overall response of nonlinear composites with complex microstructure, Computer methods in applied mechanics and engineering 157 (1-2) (1998) 69–94.

[69] A. Finel, A tetrahedron-based discretization for fft-based computational homogenization with smooth solution fields, Computer Methods in Applied Mechanics and Engineering 436 (2025) 117703.

[70] J. Crank, The mathematics of diffusion, Oxford university press, 1979.

[71] P. Ehrhart, 2.1. 4.4 diffuse scattering of x-rays or neutrons, huang scattering (dxs) 2.1. 4 experimental methods, Atomic Defects in Metals (1991) 103–103.

[72] M. Frigo, S. G. Johnson, The design and implementation of fftw3, Proceedings of the IEEE 93 (2) (2005) 216–231.

[73] A. Finel, Y. Le Bouar, B. Dabas, B. Appolaire, Y. Yamada, T. Mohri, Sharp phase field method, Physical review letters 121 (2) (2018) 025501.

[74] B. Dabas, Modeling microstructural evolution of metallic materials under extreme conditions, Thesis, Sorbonne University (2022).
URL `https://theses.hal.science/tel-03773616`

[75] R. W. Balluffi, D. N. Seidman, Diffusion-limited climb rate of a dislocation: Effect of climb motion on climb rate, Journal of Applied Physics 36 (9) (1965) 2708–2711.

[76] S. Gupta, M. Van Huis, M. Dijkstra, M. Sluiter, Depth dependence of vacancy formation energy at (100),(110), and (111) al surfaces: A first-principles study, Physical Review B 93 (8) (2016) 085432.

[77] L. Pizzagalli, M.-L. David, Surface stress calculations for nanoparticles and cavities in aluminum, silicon, and iron: influence of pressure and validity of the young-laplace equation, Materials Theory 5 (1) (2021) 5.

[78] B. Landolt, Numerical data and functional relationships in science and technology, Magnetic and Another Properties of Oxides and Related Compounds. Pt. A Garnets and perovscites (1978).

[79] S. Dais, R. Messer, A. Seeger, Nuclear-magnetic-resonance study of self-diffusion in aluminium, in: Materials Science Forum, Vol. 15, Trans Tech Publ, 1987, pp. 419–424.

[80] D. Simonovic, M. H. Sluiter, Impurity diffusion activation energies in al from first principles, Physical Review B 79 (5) (2009) 054304.

[81] T. Angsten, T. Mayeshiba, H. Wu, D. Morgan, Elemental vacancy diffusion database from high-throughput first-principles calculations for fcc and hcp structures, New Journal of Physics 16 (1) (2014) 015018.

[82] C. Jacquelin, Nanodéfauts formés sous irradiation aux électrons dans l'aluminium, Ph.D. thesis, Université Paris Saclay (COmUE) (2018).

[83] P. M. Anderson, J. P. Hirth, J. Lothe, Theory of dislocations, Cambridge University Press, 2017.

[84] F. Pedregosa, G. Varoquaux, A. Gramfort, V. Michel, B. Thirion, O. Grisel, M. Blondel, P. Prettenhofer, R. Weiss, V. Dubourg, et al., Scikit-learn: Machine learning in python, the Journal of machine Learning research 12 (2011) 2825–2830.

[85] J. Dundurs, T. Mura, Interaction between an edge dislocation and a circular inclusion, Journal of the Mechanics and Physics of Solids 12 (3) (1964) 177–189.

[86] V. Lubarda, M. Schneider, D. Kalantar, B. Remington, M. Meyers, Void growth by dislocation emission, Acta Materialia 52 (6) (2004) 1397–1408.

[87] A. Ruffini, Y. Le Bouar, A. Finel, A. I. Epishin, B. Fedelich, T. Feldmann, B. Viguier, D. Poquillon, Dislocations interacting with a pore in an elastically anisotropic single crystal nickel-base superalloy during hot isostatic pressing, Computational materials science 204 (2022) 111118.

[88] A. I. Epishin, B. S. Bokstein, I. L. Svetlov, B. Fedelich, T. Feldmann, Y. Le Bouar, A. Ruffini, A. Finel, B. Viguier, D. Poquillon, A vacancy model of pore annihilation during hot isostatic pressing of single crystals of nickel-base superalloys, Inorganic Materials: Applied Research 9 (2018) 57–65.